Thesis-1985D-C5185e

Dissertation

Chen, Ching-Yuan, 1950-

ELECTRON SPIN RESONANCE OF POINT DEFECTS IN QUARTZ

By

CHING-YUAN CHEN

Bachelor of Science
National Chung Hsing University
Taichung, Taiwan
1973

Master of Science
Oklahoma State University
Stillwater, Oklahoma
1982

Submitted to the Faculty of the
Graduate College of the
Oklahoma State University
in partial fulfillment of
the requirements for
the Degree of
DOCTOR OF PHILOSOPHY
December, 1985

ELECTRON SPIN RESONANCE OF POINT DEFECTS IN QUARTZ

Thesis Approved:

Larry E. Halliburton
Thesis Adviser

Joel J Martin

S W S McKeever

Zuhair Al-Saadi

Norman N. Durham
Dean of the Graduate College

ACKNOWLEDGEMENTS

I express my appreciation my thesis advisor, Dr. L.E. Halliburton, for his guidance, patience, encouragement, and friendship. This work would never have been completed without his assistance and support.

Appreciation is extended to Dr. J.J. Martin, Dr. E.E. Kohnke, Dr. S.W.C. Mckeever, and Dr. Z. Al-Shaeib for their instruction and their service on my commitee. The participation of Miss S.D. Tapp in the low dose and defect production mechanisms portion of this study is acknowledged. Many helpful discussions with Dr. K.L. Sweeney, Dr. K. Tanimura, and Dr. M.G. Jani are sincerely appreciated. The encouragement from Dr. L.A. Kappers and Dr. A. Halperin also made this thesis possible. I appreciate the frequent help from everyone in the instrument shop, glass shop, crystal growth laboratory, and electronics shop. The friendship of Dr. H.C. Chow, Dr. M.G. Jani, Dr. K. Tanimura, Dr. K.L. Sweeny, Dr. J. Tyminski, Dr. D. Yeh, Mr. R. Cross, Mr. R. Hantezadeh, and Mr. M. Scripsick will always be remembered.

The author wishes to express his great appreciation to everyone in his and his wife's families. The love and sacrifice from my baby, Denise, and my wife, Joanna, made this thesis complete.

Financial support from the Department of Physics, Oklahoma State University, the Air Force, and the National Science Foundation is appreciated.

TABLE OF CONTENTS

LIST OF TABLES

LIST OF FIGURES

Figure Page

CHAPTER I

INTRODUCTION

Background

Because of its high purity and excellent mechanical stability, quartz is one of the most important piezoelectric materials. High precision quartz oscillator clocks are widely used in applications ranging from microprocessors to satellite telecommunications. Problems arise in some applications because radiation changes the characteristics of the quartz by modifying pre-existing defects (formed during crystal growth) or creating new defects. These defects can cause transient and steady-state frequency changes in quartz oscillators. Thus, the development of stabilized oscillators which can operate for long periods of time requires continued investigation of defects in quartz.

It is known that crystalline SiO_2 has three polymorphic forms quartz (below 870°C), tridymite (between 870°C and 1470°C), and cristobalite (above 1470°C) (1). Additional forms only stable at high pressures are coesite and stishovite. Each has high and low forms which are slightly different in structure. Among them, low quartz is more important since it can be used in precision frequency control applications. Low quartz, is stable below 573°C while high quartz is stable between 573°C and 870°C. The transition between low and high quartz (or α and β quartz) corresponds to a small displacement of atoms with no rearrangement of the bond structure. These small atomic adjustments will transform the symmetric hexagonal β , or high-temperature, form into a slightly distorted trigonal α, or low-temperature, form on cooling. Most likely, the crystal will become electrically twinned during the transition, even though this displacive change can happen reversibly in principle.

Quartz belongs to the trigonal crystal system with point group 32(2-4); this provides an axis of threefold symmetry known as the c-axis or optical axis. Three equivalent twofold axes, separately by 120°, lie in planes perpendicular to the optical axis. The electronic structure of quartz is approximately 60% covalent and 40% ionic. It has a wide bandgap, approximately 9 eV. The α form has SiO_4 tetrahedra structures and two types of Si-O bonds, differing in length. Each oxygen is bonded to two silicons, one by a long bond and the other by a short bond, as shown in Figure 1. For α quartz at 94 K, the long and short Si-O bonds are 1.6145 Å and 1.6101 Å, respectively. Also, the cell dimensions at 94 K are $\mathbf{a}_0$ = 4.9079 Å and $\mathbf{c}_0$ = 5.3991 Å (5).

In addition to its piezoelectric property, quartz has large c-axis channels which allow interstitial ions to migrate along the channel and become trapped adjacent to substitutional impurities or other defects. Also, as a

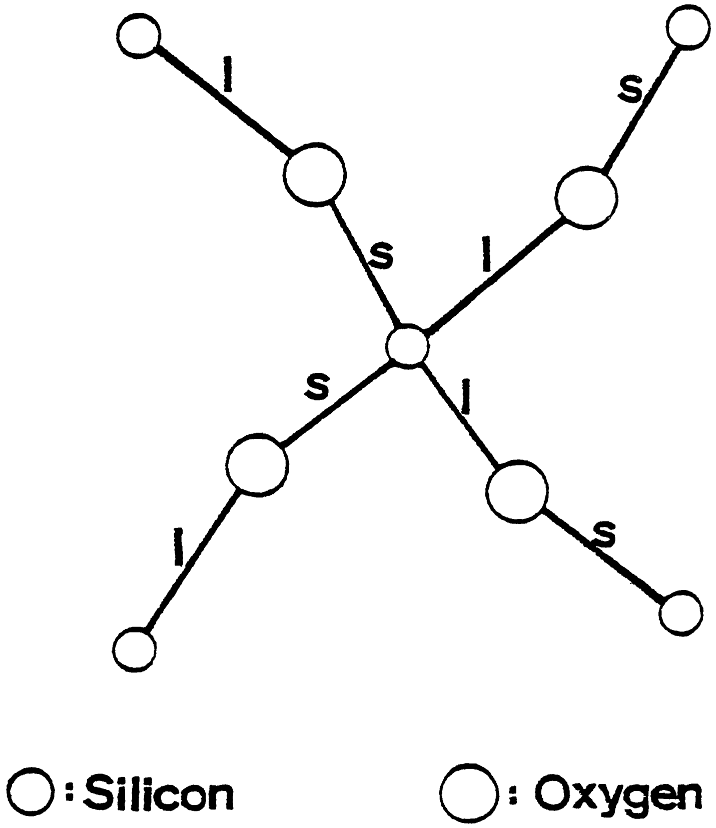

Figure 1. Partial view of the crystal structure of quartz showing the long and short bonds

result of the c-axis channel, electrodiffusion (sweeping) can be done whereby one kind of interstitial cation is replaced by another kind (6). This technique can help in understanding the point defects themselves and it also can enhance the radiation hardness of oscillators (7).

Defects in Quartz

E_1' Center

The E_1' center, one of the major radiation-induced defects in quartz, was first reported by Weeks (8) in 1956. From a consideration of the spin-lattice relaxation times, Weeks (9) suggested that the E_1' center was an electron trapped at a single silicon ion located between two oxygen vacancies. In this model, the charge neutrality was maintained with interstitial impurity ions adjacent to the E_1' center. Silsbee (10) made an angular dependence study of quartz irradiated by fast neutrons, and thus determined a set of spin-Hamiltonian parameters for the $\bar{\bar{g}}$ matrix, a strong hyperfine, and two weak hyperfine matrices. He proposed that the E_1' center was an electron concentrated primarily on one silicon (giving the strong hyperfine ~400 G splitting) and interacting weakly with two more silicons (the two weak hyperfine splittings of ~9 G and ~8 G).

Later, the theoretical studies of Feigl et al. (11) and structure calculation by Yip and Fowler (12) suggested that the E_1' center was an oxygen vacancy with one unpaired electron localized in a nonbonding sp^3 hybrid orbital centered on one of the two neighboring silicons and with a highly asymmetric relaxation of the two neighboring Si atoms. One silicon, with the extra electron, moves towards the vacancy and the other moves away from the vacancy. The ESR spectrum and the model of the E_1' center are shown in Figure 2(a) and Figure 3(a), respectively.

Recently, Jani et al. (13) correlated the migration of interstitial alkali ions, as a result of irradiation, to the production of the E_1' center. They showed a relationship between the E_1' center and the $[AlO_4]^0$ concentrations, and they also used the electron-nuclear double resonance (ENDOR) technique to verify that the two weak hyperfine interactions (8 G and 9 G splittings) were with ^{29}Si nuclei.

E_2' Center

The E_2' center, which is shown in Figure 2(b) and Figure 3(b), was discovered by Weeks and Nelson (9). The ESR spectrum has a doublet with 0.4 G splitting when the crystal's c-axis is parallel to the applied magnetic field. This leads to two possibilities, one is an electron (S = 1/2) interacting with a nucleus with spin I = 1/2 and the other is an S = 1 system. By comparing the E spectrum in crystals grown in H_2O and D_2O, it was evident that the splitting was due to a hyperfine interaction with a nearby proton(14). Besides the proton doublet, there are two additional pairs of lines with a separation of 412 G. One pair is 193.5 G above and the other is 218.5 G below the proton doublet. The separation within each of these pairs of lines is the same as the main doublet, 0.4 G. The intensity of each of these outer lines is about 0.3% of the main doublet. This suggested that these two additional pairs of lines arise from the hyperfine interaction of the defect electron with a ^{29}Si nucleus (I = 1/2). The E_2' center could be bleached at 77 K with UV light or destroyed by simply heating the sample above 150°C (9). Pairs of lines with splittings of 8 G and 9 G, such as those previously observed for the E_1' center, could not be found in the case of the E_2' center.

On the basis of these observations, Weeks suggested that the E_2' center resulted from a Si-O divacancy with the electron on a silicon ion adjacent to the oxygen vacancy. The proton is trapped nearby and the excess charge due to the remaining oxygen ions around the silicon vacancy is compensated by the monovalent (i.e., Li^+, Na^+) or divalent cation (i.e., Mg^{2+}, Ca^{2+}) impurities usually present. Jani (15) extended our knowledge of the E_2' center with an angular dependence study of the two outer pairs of lines due to the strong hyperfine interaction with ^{29}Si. However, a definite model for the E_2' center has not been proposed yet.

E_4' Center

The E_4' center was first reported by Weeks and Nelson (9). As shown in Figure 2(b), the ESR spectrum has four equally spaced, equally intense lines at X-band. This led

Weeks and Nelson to assume that the E_4' center had a hyperfine interaction with a nucleus of I = 3/2 (i.e., Li^+ or Na^+). The separation between each of the lines is about 4.8 G. Later, Haberlandt (16) suggested that the E_4' center should be fitted to a spin-Hamiltonian with S = 3/2. From observation of ^{29}Si hyperfine lines and the calculations of their principal directions for $\bar{A}_{^{29}Si(1)}$ and $\bar{A}_{^{29}Si(2)}$ at 300 K, Solentsev et al. (17) suggested a model consisting of an oxygen vacancy with a nearby interstitial H_2O.

Subsequently, Halliburton et al. (18) completed a detailed ESR study and proposed that the E_4' center has S = 1/2 with hyperfine splittings arising from one hydrogen nucleus (I = 1/2) in a situation permitting observations of all $2S(2I + 1)^2$ possible transitions. From an examination of the ESR spectrum at low microwave power levels, they found the intensity ratio of the outer pair to the inner pair, within the set of four ESR lines, was about 1.2 : 1 at 9.85 GHz. Even more important, a significant difference in this intensity ratio was seen with the use of a K-band spectrometer. This verified that the E_4' center was not an S = 1/2, I = 3/2 system. Recently, Isoya et al. (19) measured the matrices $\bar{A}_{^{29}Si(1)}$ and $\bar{A}_{^{29}Si(2)}$ at 300 K as well as $\bar{g}$, $\bar{A}_{1H}$, $\bar{A}_{^{29}Si(1)}$ and $\bar{A}_{^{29}Si(2)}$ at 40 K. They proposed that the E_4' center consisted of an oxygen vacancy between the two silicon ions, labeled Si(1) and Si(2), with a hydride ion in the vacancy and bonded to Si(1), as shown in Figure 3(c). This model was supported by _ab initio_ SCF-MO calculations, i.e., Gaussian 70, for a 15-atom cluster which yielded minimum energy configurations.

E″ Centers

The E″ centers, which are shown in Figure 2(c), were reported by Weeks and Abraham in 1965 (20). They suggested that the E″ centers were an S = 1 state resulting from a dipole-dipole interaction of two nearby electrons in S = 1/2 states. Later, these same centers were briefly described by Solentsev et al. (17). Recently, an extensive ESR study by Bossoli et al. (21) provided a more detailed description of the production and thermal decay properties of these E″ centers. They found that E″ centers could be easily produced in unswept synthetic quartz by electron irradiation at 77 K if the sample was previous irradiated at room temperature. From their pulse anneal studies, they showed that the E_2'' centers anneal near 50°C while the E_1'' and E_3'' centers were more stable and anneal near 85°C and 95°C, respectively.

The large angular dependence of the doublet separations suggested that these centers are S = 1 spin systems. The alternative candidate, S = 1/2 and I = 1/2 (100% abundance) was ruled out by the observations by Bossoli et al. (21) of the 'half-field', $\Delta m_s = \pm 2$, transition. They suggested that the E_1'' centers were two oxygen vacancies each with a single unpaired electron. In other words, this is equivalent to two neighboring E_1' centers. This view was supported by the

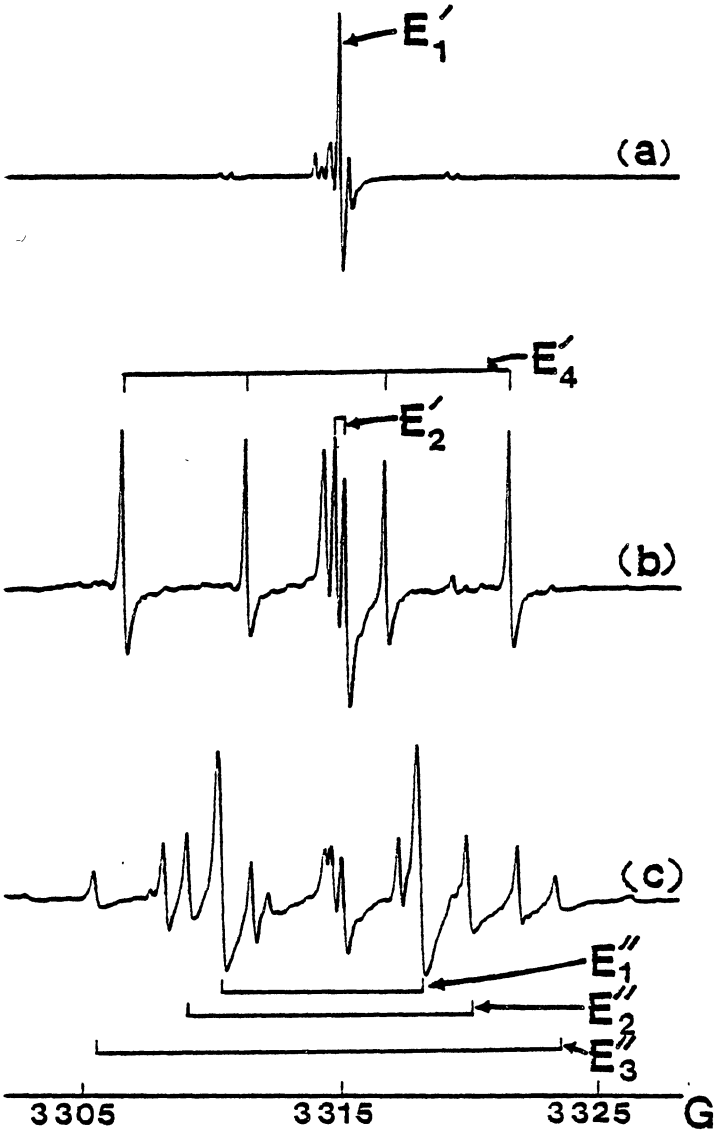

Figure 2. ESR spectra of E_1', E_2', E_4', and E'' centers

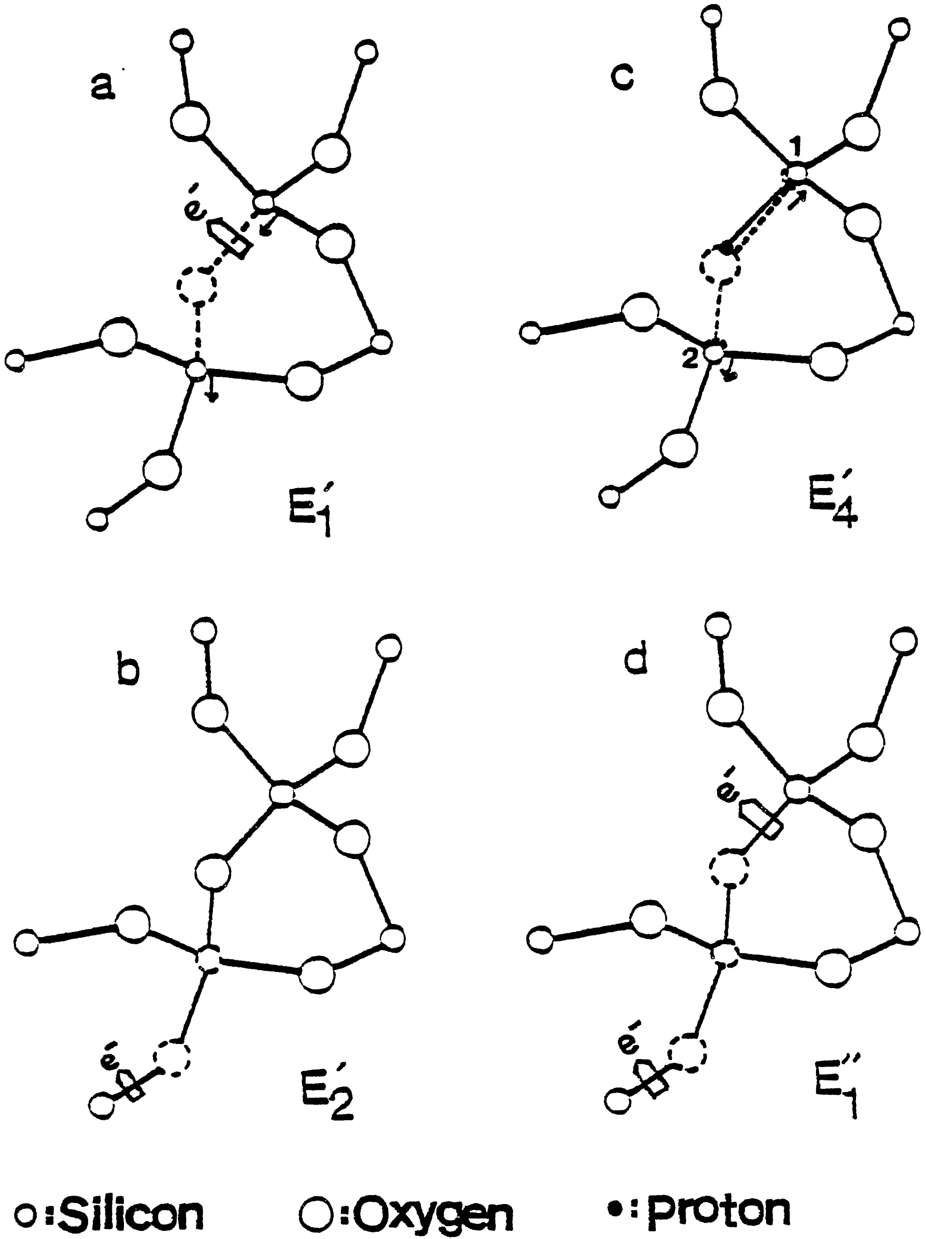

Figure 3. Proposed models for E_1', E_2', E_4', and E_1'' by Yip and Fowler, Weeks, Isoya et al., and Jani and Halliburton, respectively. The arrow indicates the relaxation of the ions. The proton is not specified in (b)

two slightly inequivalent strong ^{29}Si hyperfine interactions observed for each of the E$''$ centers. Jani (22) suggested that two oxygens and a silicon were missing and two electrons were in the sp^3 hybrid orbitals extending from Si(1) and Si(2) for the E_1'' centers, as shown in Figure 3(d). So far, a definite model has not been proposed for these centers.

Al-Associated Centers

When an aluminum ion (Al^{3+}) substitutes for a silicon ion (Si^{4+}), overall charge neutrality requires a positive entity to act as a compensator for the aluminum. Alkali ions (i.e., Li^+ and Na^+) and protons, which are small, can diffuse through the open channels of the c-axis and locate at interstitial sites adjacent to the substitutional aluminum ions (23). A hole trapped at an oxygen ion adjacent to the aluminum ion after ionizing radiation forms the defects known as the $[AlO_4]^\circ$ centers. Another three hole centers, labeled $[AlO_4/H^+]^+$, $[AlO_4/Li^+]^+$, and $[AlO_4/Na^+]^+$, are formed after irradiation at 77 K if the substitutional aluminum ions were compensated by monvalent ions. Figure 4 shows the $[AlO_4/H^+]^+$, $[AlO_4/Li^+]^+$, $[AlO_4/Na^+]^+$, and $[AlO_4]^\circ$ centers. The notation which we use was proposed by Weil (24).

The $[AlO_4]^\circ$ centers were first reported by Griffiths, Owen, and Ward (25) and was interpreted theoretically by O'Brien (26). The ESR spectrum covers ~30 G at 77 K as a result of a hyperfine structure due to the ^{27}Al nucleus (I =

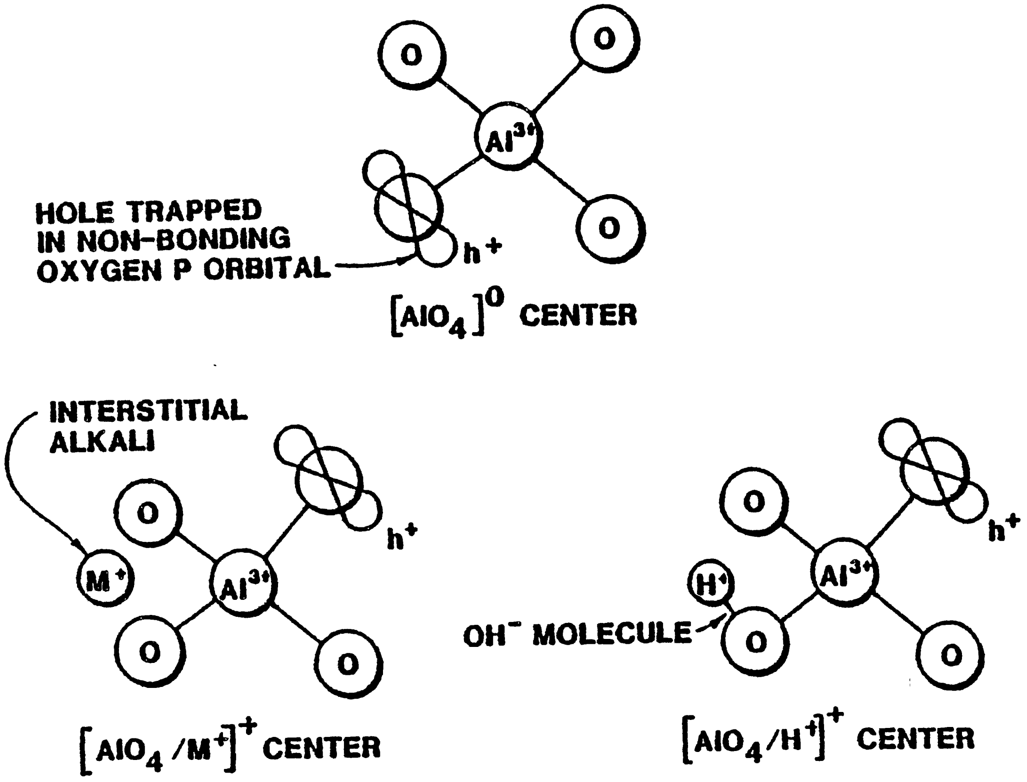

Figure 4. Models for aluminum-hole centers

5/2, 100% abundance). The accepted model for the $[AlO_4]^0$ centers consists of a hole trapped in a nonbonding p orbital on one of two equivalent oxygens with long bonds adjacent to the aluminum ion (5). The excited state of this center has the hole on one member of the other pair of equivalent oxygens (i.e., the short-bond side). Schnadt and Schneider (27) determined that the thermal activation energy between the ground state (long bond) and the excited state (short bond) is 30 meV. The ESR line-width of the $[AlO_4]^0$ centers is strongly temperature dependent and they are too broad to observe above 170 K. This line broadening arises from a thermally activated hopping of the hole among the different oxygens surrounding the substitutional aluminum.

The $[AlO_4]^0$ centers shown in Figure 5(c), have been studied in detail during the past 20 years (28-34). One striking effect was discovered by Markes and Halliburton (35) while monitoring the ESR spectrum of the $[AlO_4]^0$ centers during a sequence of irradiations and thermal anneals. They found that the initial 77 K irradiation of unswept samples failed to produce many $[AlO_4]^0$ centers. However, a subsequent intermediate room-temperature irradiation caused interstitial alkali ions to become mobile and migrate away from the aluminum ions. This allows the substitutional aluminum ions to trap holes and produce a large concentration of $[AlO_4]^0$ centers. With this discovery, the effect of sweeping and the concentration of aluminum can be evaluated. It is well known that the formation of $[AlO_4]^0$ centers by radiation is directly related to changes in the acoustic loss spectrum of quartz resonators. King and Martin (6, 36, 37) suggested that the acoustic loss peaks at 100 K and 135 K in 5 MHz, 5th overtone, AT-cut resonators were due to $[AlO_4]^0$ centers.

The two perturbed aluminum-associated hole centers shown in Figure 5(a,b) were observed and studied initially by Mackey (38) and later in more detail by Nuttall et al. (39). Recently, these centers were discussed by Mckeever et al. (40) as a part of a study of natural Alaska quartz containing Ge and Ti. In this latter case, the perturbed $[AlO_4/Li^+]^+$ and $[AlO_4/H^+]^+$ centers were formed by irradiation with the electrons being trapped at the substitutional germanium ion sites, as shown in Figure 5(a). When the irradiated sample was warmed to a temperature higher than 200 K (a critical temperature in quartz studies), the perturbed aluminum-hole centers decayed and converted into $[AlO_4]^0$ centers (unperturbed). Also, two other centers (Li^+-Ge^{4+}-e^- and Ti^{3+}-H^+) grew in as shown in Figure 5(c). This can be explained by having the alkali ions and protons migrate from the aluminum ion to other lattice sites (i.e., Ge^{4+}, Ti^{3+} ...) when the temperature is high enough to allow them to become mobile. However, in samples with very little Ge and Ti, few aluminum-associated perturbed centers were found. This last observation can be explained as a lack of electron traps. In the perturbed aluminum-hole centers, a six-line hyperfine pattern arises from the interaction of

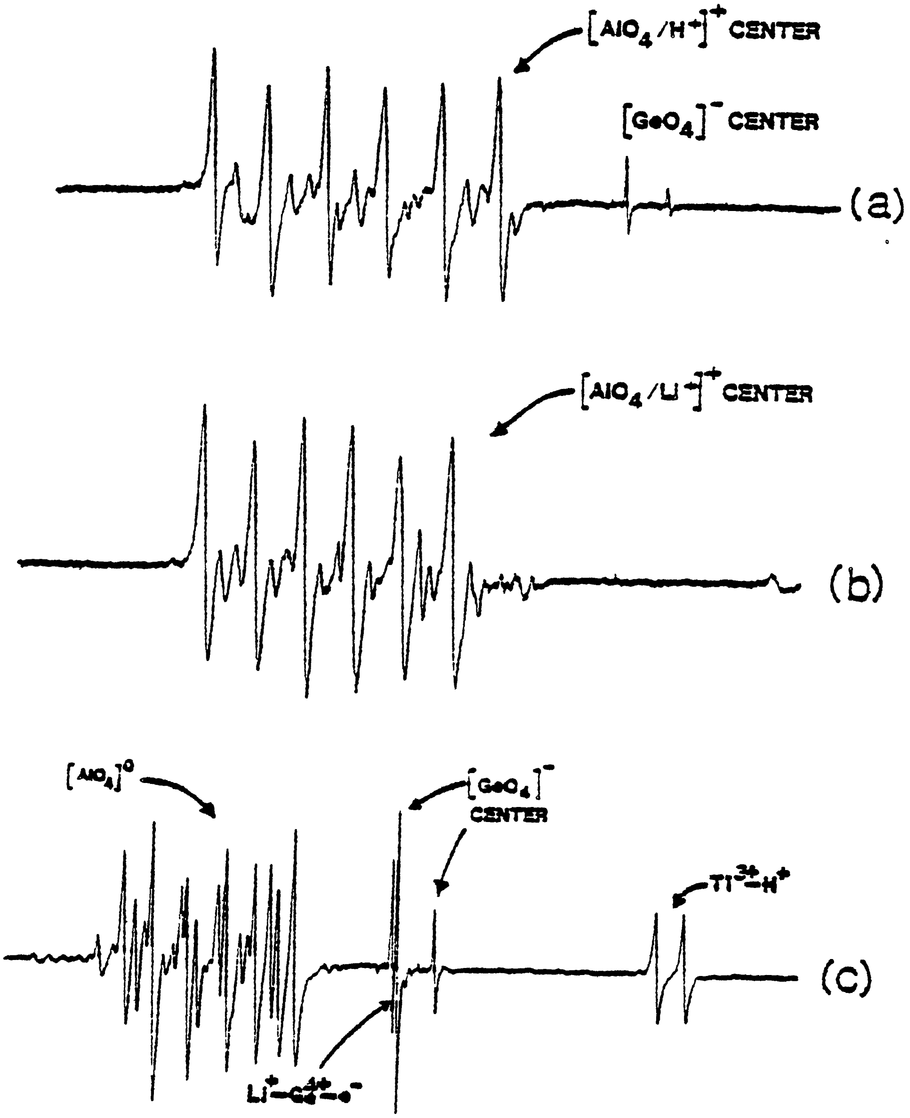

Figure 5. ESR spectra of aluminum-hole centers, germanium elertron traps, and titanium centers

the unpaired electron with a single aluminum nucleus (I = 5/2, 100% abundance).

The double-hole centers $[AlO_4]^+$ have a hole trapped at two of the oxygen ions neighboring the substitutional aluminum ion. This results in a triplet (S = 1) spin system. The double-hole centers have been characterized by Nuttall at al. (41).

Present Study

After the introductory chapters, the new research results are divided into three parts. In Chapter V, the production of point defects by low doses of radiation are described for a series of commercially available quartz samples. Electron spin resonance was used to identify and monitor the paramagnetic defects produced by doses ranging from approximately 700 rads up to several Mega-rads. Both unswept and hydrogen-swept quartz were included in this portion of the study, and comparisons were made between samples irradiated at 77 K and at room temperature. From this data it appears that there is no simple correlation between the response of quartz to low and high levels of radiation. Also, possible mechanisms which lead to the radiation-induced dissociation of hydrogen and alkali ions from aluminum sites are described (42).

Three radiation-induced hydrogen-related centers (labeled H-1, H-2, and H-3) along with $[H_3O_4]^0$ centers are discussed in Chapter VI. Instead of low doses, heavy doses were used to produce the H-1, H-2, and H-3 centers. Results from thermal anneal studies for the H-1, H-2, H-3, hydrogen atom, and $[H_3O_4]^\circ$ centers provide information about relations between them. The ESR angular dependence study of the H-2 and H-3 centers suggest possible models for these defects.

In Chapter VII, two additional hydrogen-associated centers, labeled U-2 and U-3, are discussed. The U-2 and U-3 centers were first reported by Markes and Halliburton (35) in 1979. In the present study, thermal anneal results for the U-2, U-3, and H° centers were repeated and the angular dependence data were taken for the U-3 centers. From this data, a possible models for these centers are proposed.

CHAPTER II

THEORY OF ELECTRON SPIN RESONANCE

Unlike various types of optical spectroscopy which use time-varying electric fields to induce dipole transitions, electron spin resonance arises from the magnetic dipole transitions induced by time-varying magnetic fields. It has been forty years since the discovery of ESR by Zavoiskii (42) and the technique is now widely used. This spectroscopic method evolved from the fundamental Stern-Gerlach experiment which described the phenomenon of space quantization of the atoms in a magnetic field. Subsequently, Uhlenbeck and Goudsmit introduced a new electron spin quantum number, S, to link the electron spin with the electron magnetic moment (43-46).

Electron Zeeman Interaction

The magnetic moment of a free electron can be related to the spin angular momentum, or electron spin, as:

$$\bar{\mu}_s = \gamma \bar{P} = \gamma (h/2\pi) \bar{S} = -g \beta \bar{S} \qquad (2\text{-}1)$$

where μ_s is the magnetic moment of a free electron,

P is the angular momentum of a free electron,

γ is the magnetogyric ratio, eh/2mc,

h is Plank's constant,

S is the electron spin which has two quantum state, $m_s = +1/2$ and $m_s = -1/2$,

β is the Bohr magneton, $h\gamma/2$,

g is the g factor for a free electron which is 2.002319278,

and the negative sign in equation 2-1 comes from the negative charge of the electron.

In a static magnetic field, the interaction between the magnetic moment of the electron and an applied magnetic field leads to a quantization of the energy levels of the system due to the space quantization of the electron spin angular momentum. The interaction energy can be expressed as

$$E = \overline{\mu}_s \cdot \overline{H} = -g\beta\, \overline{S} \cdot \overline{H} \qquad (2\text{-}2)$$

Let the quantization of the spin angular momentum be along the direction of the magnetic field, which is taken as the Z-axis. Then the interaction energy becomes

$$E = -g\beta H_z m_s \qquad (2\text{-}3)$$

The only possible values for m_s are +1/2 and -1/2 and there are two corresponding energy levels, referred to as Zeeman levels. The energy difference between these two electron spin states (two Zeeman levels) is given as

$$\Delta E = g\beta H. \tag{2-4}$$

This separation energy ΔE increases linearly with the magnetic field. A transition can be induced between these two electron spin states when the energy of one quantum of electromagnetic radiation matches this energy difference ΔE. By using the Plank-Einstein equation, this relation can be expressed as

$$\Delta E = g\beta H_r = h\nu. \tag{2-5}$$

Here H_r represents the resonance magnetic field and ν is the frequency of the incident photon.

From perturbation theory in quantum mechanics, the probability for the transition between $m_S = +1/2$ and $m_S = -1/2$ states is given as

$$W_{\frac{1}{2}\leftrightarrow-\frac{1}{2}} = (\pi g^2\beta^2/2h^2)H_\perp^2[S(S+1)-m_S(m_S-1)]g(\omega-\omega_o) \tag{2-6}$$

Here $H_\perp$ is the amplitude of the high frequency magnetic electromagnetic field, ω is the angular frequency, and $g(\omega-\omega_o)$ is the line-shape function. From the equation above, the transition can occur only when the electromagnetic radiation is polarized such that the oscillating magnetic field has a component perpendicular to the static magnetic field. Thus, transitions between electron spin states can be driven by the electromagnetic radiation.

Figure 6(a) gives a brief summary of the electron Zeeman effect. It illustrates the two Zeeman levels corresponding to S = 1/2 and the resulting single ESR line. The selection rule for the transition is $\Delta m_S = \pm 1$.

Nuclear Zeeman Interaction

The theory which we discussed in the previous section for the electron spin system can be applied to the nuclear spin system. Since the nuclear magnetic moments are about 10^{-3} of the electron magnetic moments, the resonance frequencies are in the MHz range instead of the GHz range normally used for the electron Zeeman resonance. Thus, instead of using microwave radiation, a radio-frequency field is used to induce the transitions between nuclear spin states. The Hamiltonian for the nuclear Zeeman interaction is

$$\overline{\mathcal{H}} = -g_N \beta_N \bar{H} \cdot \bar{I} \tag{2-7}$$

where g_N is the nuclear g factor, $\beta_N = eh/4\pi m_N c$ is the nuclear magneton, m_N is the proton mass, and I is the nuclear spin. The corresponding nuclear Zeeman levels, when the nuclear spin angular momentum is quantized in the direction of the applied field, are

$$E = -g_N \beta_N H m_I. \qquad (2\text{-}8)$$

Here m_I is the nuclear spin quantum number. The separation energy for the transitions is $\Delta E = h\nu = g_N \beta_N H_r$ and the selection rule is $\Delta m_I = \pm 1$, which is similar to the electron Zeeman transition, $\Delta m_s = \pm 1$. Nuclear magnetic resonance is a powerful technique for use in the study of solids.

Nuclear Hyperfine Interaction

When an unpaired electron is in the vicinity of a magnetic nucleus, the interaction between this electron and the nearby nucleus is called the nuclear hyperfine interaction. There are two types of hyperfine interactions, one is dipolar (anisotropic) and the other is Fermi-contact (isotropic).

The isotropic hyperfine interaction arises from the finite probability of finding the electron at the nucleus. Fermi(47) calculated this isotropic interaction energy approximately as

$$E_{\mathrm{ISOTROPIC}} = (-8\pi/3)\,|\psi(0)|^2\,\bar{\mu}_S \cdot \bar{\mu}_I. \qquad (2\text{-}9)$$

Here $\psi(0)$ is the electronic wavefunction at the nucleus and $\bar{\mu}_S$ and $\bar{\mu}_I$ are the electron magnetic dipole and nuclear magnetic dipole, respectively. The Hamiltonian can be written as

$$\bar{\mathcal{H}} = (8\pi/3)g\beta g_N\beta_N|\psi(0)|^2\bar{S}\cdot\bar{I} = hA_o\bar{S}\cdot\bar{I} \tag{2-10}$$

by using $\mu_{S_z} = -g\beta S_z$, $\mu_{I_z} = g_N\beta_N I_z$. The parameter A_o is called the hyperfine coupling constant and hA_o the interaction energy between the electron and the nucleus.

Classically, the dipole-dipole interaction between an electron magnetic dipole $\bar{\mu}_S$ and a nuclear magnetic dipole $\bar{\mu}_I$ is given by

$$E_{DIPOLE} = (\bar{\mu}_S\cdot\bar{\mu}_I)/r^3 - 3(\bar{\mu}_S\cdot\bar{r})(\bar{\mu}_I\cdot\bar{r})/r^5 \tag{2-11}$$

where $\bar{r}$ is the vector between $\bar{\mu}_S$ and $\bar{\mu}_I$. Again, the Hamiltonian can be expressed as

$$\bar{\mathcal{H}} = -g\beta g_N\beta_N[(\bar{S}\cdot\bar{I})/r^3 - 3(\bar{S}\cdot\bar{r})(\bar{I}\cdot\bar{r})/r^5] \tag{2-12}$$

By expanding equation (2-12), the Hamiltonian can be expressed as

$$= (-g\beta g_N\beta_N) *$$

$$[S_X, S_Y, S_Z] \begin{bmatrix} \left\langle\frac{r^2-3x^2}{r^5}\right\rangle, & -\left\langle\frac{3xy}{r^5}\right\rangle, & -\left\langle\frac{3xz}{r^5}\right\rangle \\ -\left\langle\frac{3xy}{r^5}\right\rangle, & \left\langle\frac{r^2-3y^2}{r^5}\right\rangle & -\left\langle\frac{3xz}{r^5}\right\rangle \\ -\left\langle\frac{3xy}{r^5}\right\rangle, & \left\langle\frac{3yz}{r^5}\right\rangle, & \left\langle\frac{r^2-3z^2}{r^5}\right\rangle \end{bmatrix} \begin{bmatrix} I_X \\ I_Y \\ I_Z \end{bmatrix}$$

$$= h\bar{S}\cdot\overleftrightarrow{T}\cdot\bar{I} \tag{2-13}$$

where the angular brackets imply an average taken over the electronic wavefunction. By adding the Fermi-contact (isotropic) and the dipolar (anisotropic) terms, the hyperfine interaction is given as

$$\overline{\mathcal{H}} = hA_0\bar{S}\cdot\bar{I} + h\bar{S}\cdot\overset{\leftrightarrow}{T}\cdot\bar{I} = h\bar{S}\cdot\overset{\leftrightarrow}{A}\cdot\bar{I}. \qquad (2\text{-}14)$$

Here $\overset{\leftrightarrow}{A} = A_0\bar{1} + \overset{\leftrightarrow}{T}$.

Finally we combine the electron Zeeman, nuclear Zeeman, and nuclear hyperfine interactions together, the full Hamiltonian will be

$$\overline{\mathcal{H}} = \beta\bar{S}\cdot\overset{\leftrightarrow}{g}\cdot\bar{H} + h\bar{S}\cdot\overset{\leftrightarrow}{A}\cdot\bar{I} - g_n\beta_n\bar{I}\cdot\bar{H} \qquad (2\text{-}15)$$

For example, with one unpaired electron interacting with a nucleus of nuclear spin I = 1/2, there will be four spin states. The four energy levels are

$$\begin{aligned}
E &= \langle +1/2,+1/2|\mathcal{H}|+1/2,+1/2\rangle = (+1/2)g\beta H + hA/4\\
E &= \langle +1/2,-1/2|\mathcal{H}|+1/2,-1/2\rangle = (+1/2)g\beta H - hA/4\\
E &= \langle -1/2,+1/2|\mathcal{H}|-1/2,+1/2\rangle = (-1/2)g\beta H - hA/4\\
E &= \langle -1/2,-1/2|\mathcal{H}|-1/2,-1/2\rangle = (-1/2)g\beta H + hA/4 \quad (2\text{-}16)
\end{aligned}$$

These four energies levels and the transitions given by this selection rules, $\Delta m_s = \pm 1$ and $\Delta m_I = 0$ are shown in Figure 6(b). This is the spin Hamiltonian used throughout this dissertation.

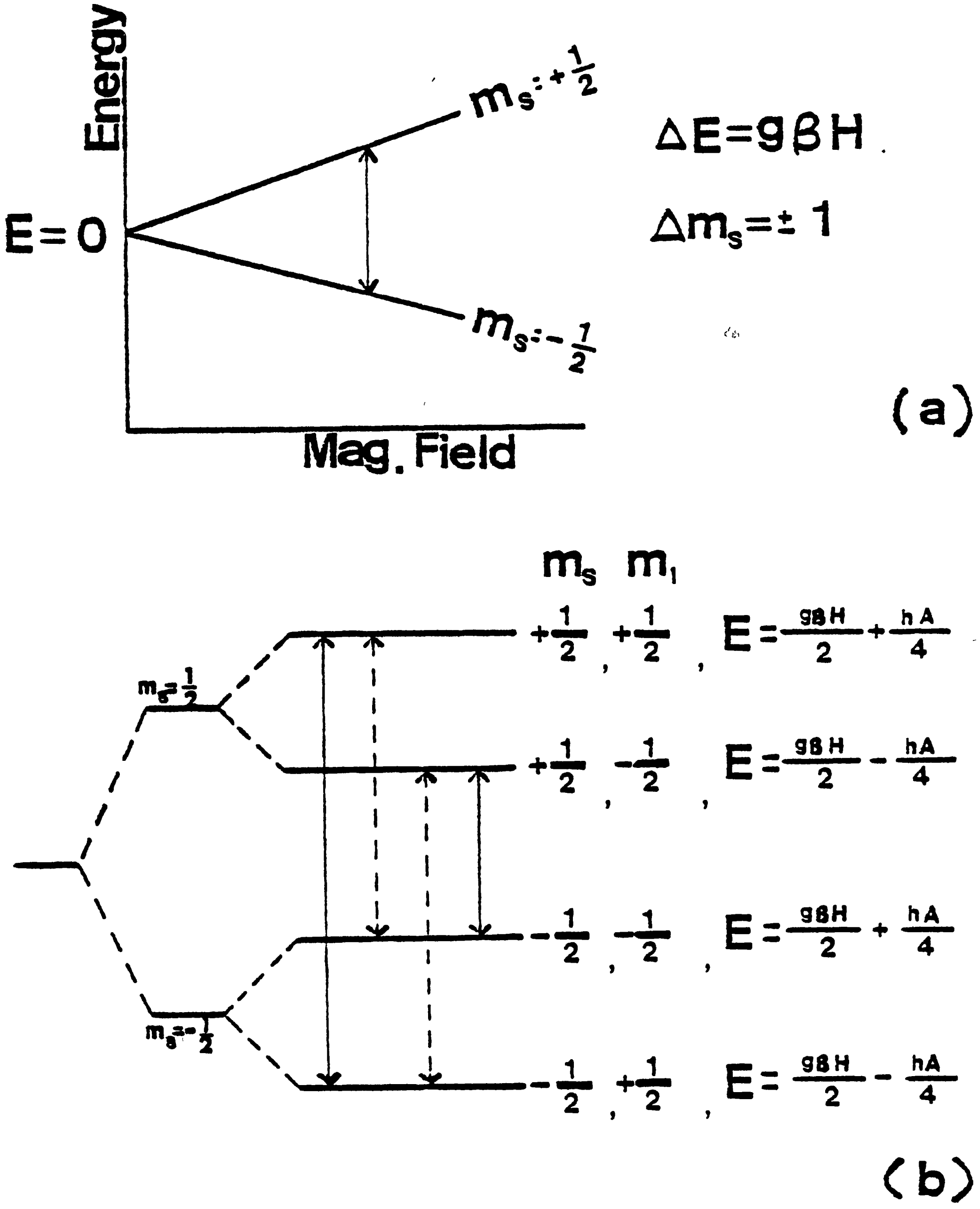

Figure 6. Part (a) shows the two Zeeman levels corresponding to S=1/2 and the resulting single ESR line
Part (b) shows the four energy levels due to an S=1/2, I=1/2 system and the allowed (solid) and forbidden (dashed) transitions, respectively

CHAPTER III

EXPERIMENTAL APPARATUS AND PROCEDURE

Sample Preparation and Defect Production

The quartz crystals used in this study were obtained from Sawyer Research Products and Thermodynamics. No major differences were observed in the samples from these two sources. For our ESR studies, the samples were cut to dimensions of 8 mm x 2.5 mm x 3 mm in the X, Y and Z directions, respectively, by using a diamond saw in the Crystal Growth Laboratory of Oklahoma State University. All samples were taken from the Z-growth region. The aluminum content of our quartz samples varied from $\sim$1 ppm to $\sim$10 ppm. In addition to aluminum, other impurities were present including lithium, sodium, hydrogen, and germanium. These latter ions acted either as charge compensators or as electron traps in the quartz crystal.

Samples were either irradiated with 1.7 MeV electrons from a Van de Graaff accelerator (beam current of 10 μA) or in a ^{60}Co gamma cell (5.5 rads per second). For irradiation at 77 K, the sample was put inside a styrofoam cup filled with liquid nitrogen. The cup was placed on an aluminum stand approximately one inch from the window of the accelerator tube or was lowered directly into the gamma cell.

ESR Spectrometer

All ESR measurements were made on an IBM Instruments (Bruker) ER200D X-band homodyne spectrometer either at liquid helium, liquid nitrogen, or room temperature. This spectrometer consists of a magnet, a magnet power supply, a microwave bridge, and a separate console, containing a timebase unit, a signal channel, a field controller, and a chart recorder. A TE 102 rectangular cavity was used in our study. This commercial cavity is equipped with Helmholtz coils for 100 kHz modulation.

Figure 7 is a block diagram of the microwave bridge. It contains all the components which generate, control, and detect the microwave radiation. A klystron produces coherent microwaves. These microwaves are then divided between a sample arm and a reference arm. In the sample arm, a microwave attenuator controls the microwave power and a nonreciprocal microwave circulator directs the microwaves to the cavity and also the reflected signal from the cavity to the detector. The reference arm contains an attenuator and a phase shifter to vary the detector bias. The biasing power is controlled by the attenuator while the phase shifter is used for phase adjustment. Frequency stability of the microwave source is achieved by locking the klystron frequency to the cavity resonant frequency. If any frequency mismatch occurs, a small error voltage is

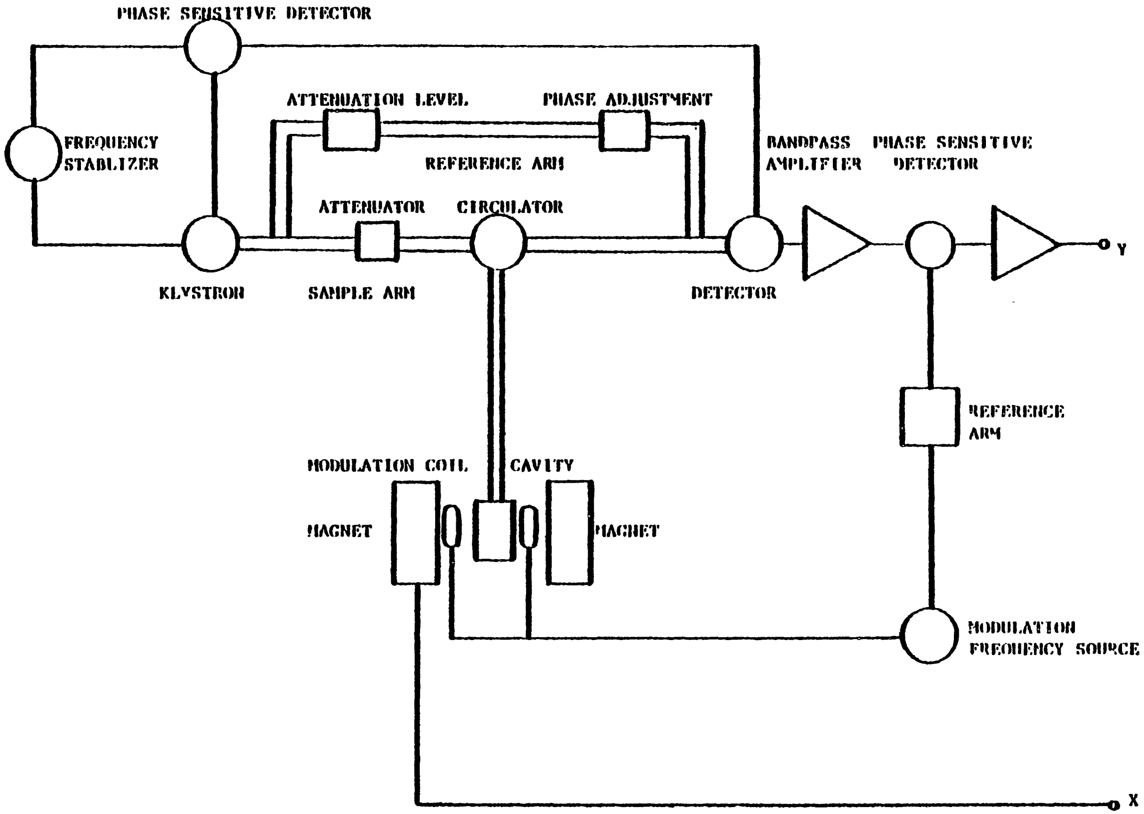

Figure 7. Block diagram of the electron spin resonance spectrometer

produced. This error signal is amplified and applied to the klystron reflector voltage to force the klystron to the cavity frequency. To aid in detecting the ESR signals, the magnetic field is modulated at 100 kHz via coils mounted on the cavity. The 100 kHz signal from the microwave detector diode is fed to the phase sensitive amplifier. This amplifier improves the signal-to-noise ratio by amplifying only the signal at the modulation frequency and in phase with it. The output signal is displayed on the oscilloscope of the time base unit (ER001) or is plotted by the chart recorder mounted in the console as the magnetic field is swept across the region of interest.

Magnetic fields were measured by a Varian E-500 Gaussmeter. The NMR probe contained a proton sample in a coil which is a part of the resonant circuit of a marginal oscillator. A rigid BNC connector is used to connect the probe to the marginal oscillator. The other end of the probe is locked in a position between the probe faces of the magnet. A standard Cr^{3+}-doped MgO sample was used to correct the measured field values since the position of the probe was not the same as the sample in the ESR cavity. The known g-value of the standard sample is 1.9799. A Hewlett Packard frequency counter 5340A is connected directly to the microwave bridge of the ESR spectrometer to give 7-digit frequency values.

Thermal Anneal Procedures

Variable temperature pulse anneals were done independently outside the ESR spectrometer using a nitrogen gas flow system. Figure 8 shows the experimental set-up for these thermal anneals. The desired temperature of the gas, and thus the sample was achieved by first cooling the gas with a heat exchanger immersed in a liquid nitrogen bath and then passing the gas through a transfer tube containing an electric heater. A Bruker ER16801 variable temperature Dewar equipped with a copper-vs-constantan thermocouple is connected to the other end of the transfer tube. The final temperature of the gas was monitored with a Hewlett Packard 3465A digital multimeter.

By using the Varian 4546 heater controller and also adjusting the flow of nitrogen gas, the samples were held at desired temperatures for five minutes. Then, the sample was returned to the microwave cavity for monitoring of the ESR spectra. When the experiment was done with a 77 K base temperature, the sample was mounted in a teflon holder at the end of a hollow stainless steel rod. A home-made finger Dewar, primarily Pyrex but with a quartz tip, was used to accommodate the stainless steel rod with the sample. The Dewar has a cover with angle markings for use with a pointer on the top of the rod, and a rough angular dependence study can be done by rotating the rod to the desired angle markings.

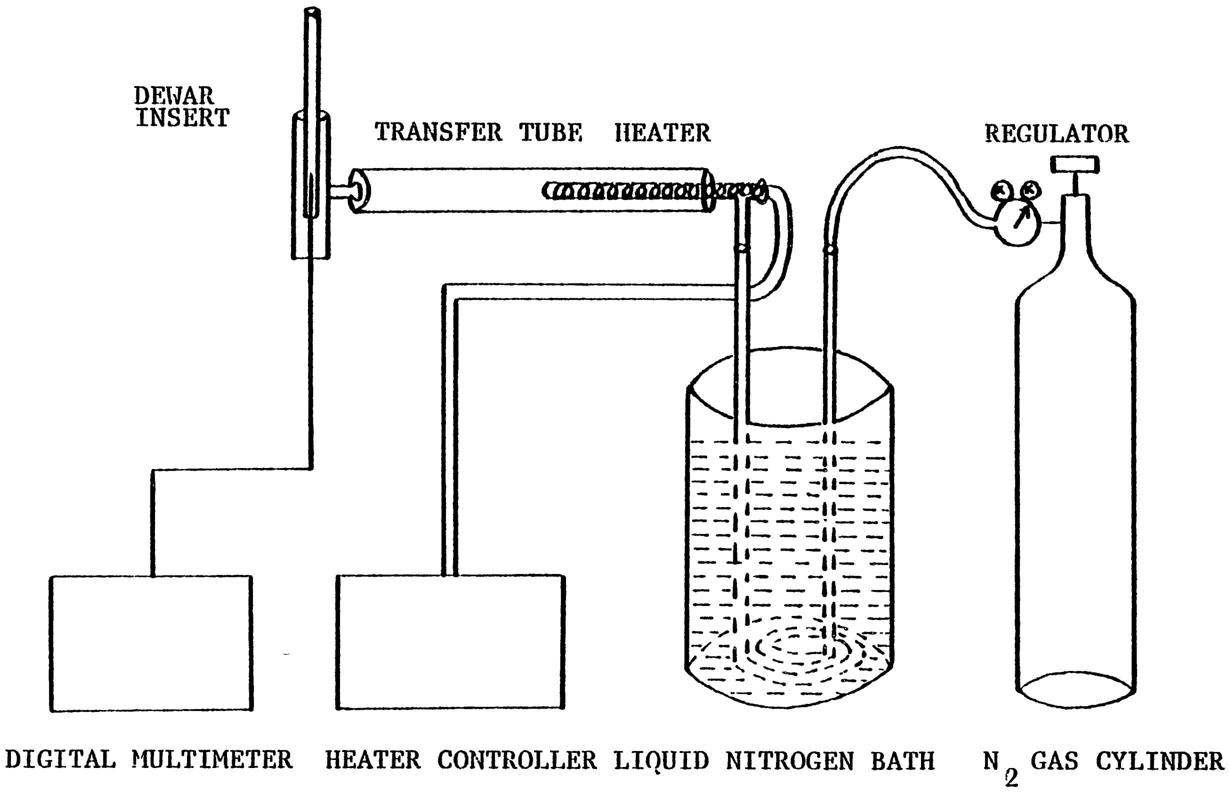

Figure 8. Apparatus for pulsed thermal anneal experiments

Helium Temperature Procedures

Figure 9 shows the liquid transfer Heli-Tran system which provides refrigeration in the temperature range between 4.2 K and 300 K via a controlled transfer of liquid helium. The helium Dewar cavity insert and the flexible transfer line were evacuated to a vacuum of 10^{-5} Torr or less to maintain a high efficiency of helium flow to the sample in the cavity. A valve at the cavity end of the Heli-Tran was used to control the helium flow rate. An Air Products model 3700 digital temperature indicator/controller was used to regulate the temperature.

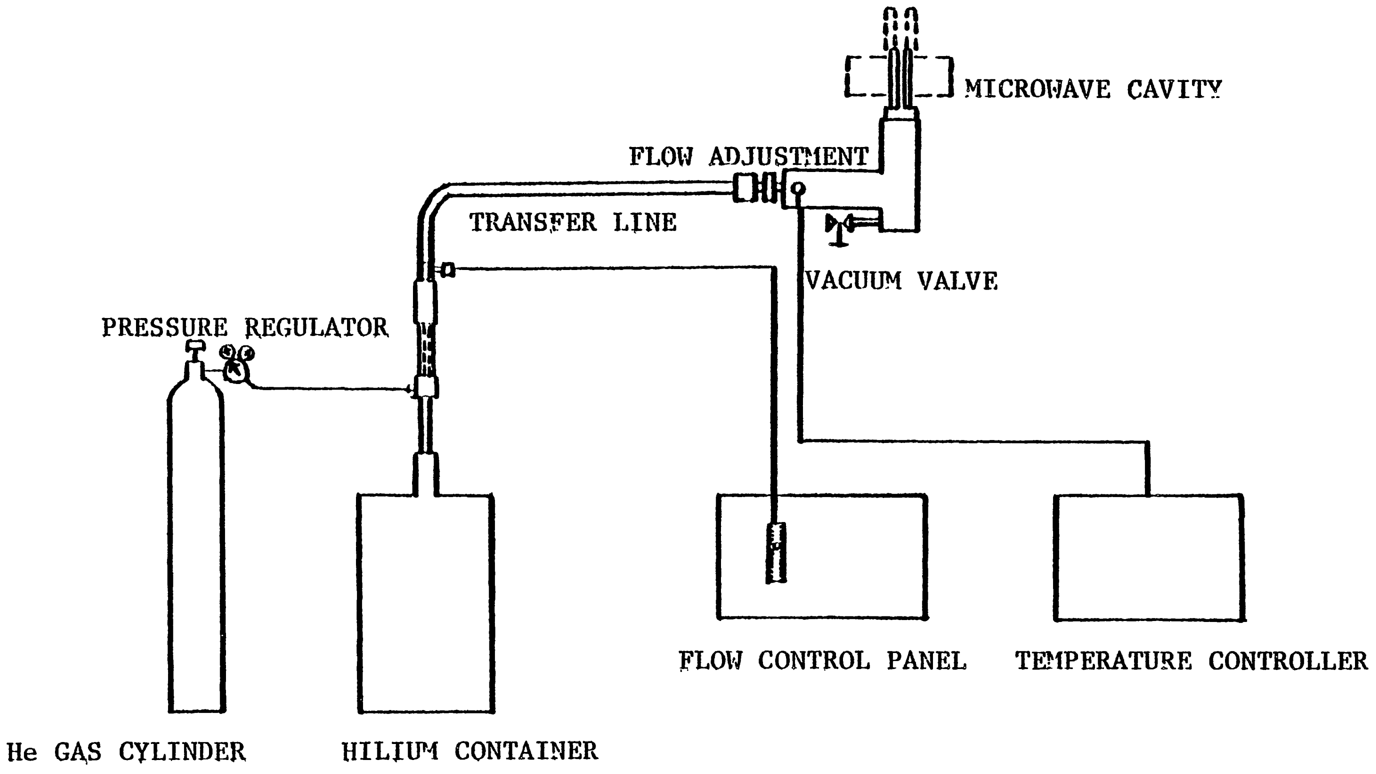

Figure 9. Apparatus for liquid helium temperature experiments

CHAPTER IV

THEORETICAL ANALYSIS

The general spin Hamiltonian which describes a system with electron spin S = 1/2 and nuclear spin I = 1/2 is

$$\overline{\mathcal{H}} = \beta \bar{S} \cdot \overleftrightarrow{g} \cdot \bar{H} + h\bar{S} \cdot \overleftrightarrow{A} \cdot \bar{I} - g_N \beta_N \bar{I} \cdot \bar{H} \qquad (4\text{-}1)$$

The first term represents the electron Zeeman interaction, the second term represents the nuclear hyperfine interaction, and the last term is the nuclear Zeeman interaction. These interactions were discussed in chapter II.

The coordinate systems defined below are used to convert the spin Hamiltonian into a suitable form for computer programming.

x, y, z: a coordinate system with the magnetic field along the z-axis

x_c, y_c, z_c: Crystal coordinate system

x_1, y_1, z_1: Principal coordinate system for the hyperfine matrix $\overleftrightarrow{A}$

x_g, y_g, z_g: Principal coordinate system for the $\overleftrightarrow{g}$ matrix

By using these four coordinate systems, the Hamiltonian can be rewritten as:

$$\mathcal{H} = \beta\,[g_x S_{x_g} H_{x_g} + g_Y S_{Y_g} H_{Y_g} + g_z S_{z_g} H_{z_g}] + h[A_x S_{x_1} I_{x_1} + A_Y S_{Y_1} I_{Y_1} + A_z S_{z_1} I_{z_1}] - g_N \beta_N H I_z \qquad (4\text{-}2)$$

To transform the principal coordinate systems for the $\overleftrightarrow{g}$ and $\overleftrightarrow{A}$ matrices to the magnetic field coordinate system, we need to have two 3 x 3 rotation matrices [TG] and [TH] which are defined as

$$\begin{bmatrix} x_g \\ y_g \\ z_g \end{bmatrix} = \begin{bmatrix} & & \\ & TG & \\ & & \end{bmatrix} \begin{bmatrix} x \\ y \\ z \end{bmatrix} \quad \text{and} \quad \begin{bmatrix} x_1 \\ y_1 \\ z_1 \end{bmatrix} = \begin{bmatrix} & & \\ & TH & \\ & & \end{bmatrix} \begin{bmatrix} x \\ y \\ z \end{bmatrix}$$

The spin and the magnetic field transform in the same manner, i.e.,

$$\begin{bmatrix} S_{x_g} \\ S_{Y_g} \\ S_{z_g} \end{bmatrix} = \begin{bmatrix} & & \\ & TG & \\ & & \end{bmatrix} \begin{bmatrix} S_x \\ S_Y \\ S_z \end{bmatrix} \quad \text{and} \quad \begin{bmatrix} H_{x_g} \\ H_{Y_g} \\ H_{z_g} \end{bmatrix} = \begin{bmatrix} & & \\ & TG & \\ & & \end{bmatrix} \begin{bmatrix} 0 \\ 0 \\ H \end{bmatrix}$$

Then, the Hamiltonian can be transformed to the magnetic coordinate system (x, y, z) where it is expressed as

$$\begin{aligned}\mathcal{H} = {} & W3S_z+[(W1-iW2)/2]S_+ && + [(W1+iW2)/2]S_- \\ & +[(W4-W7-2iW5)/4]S_+I_+ && + [(W4+W7)/4]S_+I_- \\ & +[(W4+W7)/4]S_-I_+ && + [(W4-W7+2iW5)/4]S_-I_- \\ & +[(W6-iW8)/2]S_+I_z && + [(W6+iW8)/2]S_-I_z \\ & +[(W6-iW8/2]S_zI_+ && + [(W6+iW8)/2]S_zI_- \\ & +W9S_zI_z-g_N\beta_N I_z. \end{aligned} \qquad (4\text{-}4)$$

The Hamiltonian can be further simplified as

$$\begin{aligned} & =W3S_z+Q1^*S_++Q1S_-+Q2^*S_+I_++Q2S_-I_-+Q3S_-I_++Q3S_+I_-+ \\ & Q4^*S_+I_z+Q4S_-I_z+Q4^*S_zI_++Q4S_zI_-+W9S_zI_z-g_n\beta_n HI_z \end{aligned} \qquad (4\text{-}5)$$

where

$Q1 = (W1 + iW2)/2$

$Q2 = (W4 - W7 + 2iW5)/4$

$Q3 = (W4 + W7)/4$

$Q4 = (W6 + iW8)/2.$

Equation (4-5) is the Hamiltonian we will use for our systems with $S = 1/2$ and $I = 1/2$ to find the Hamiltonian matrix elements. With this spin system, we will have a basis of $|m_S, m_I>$ representing the four eigenvectors. Thus, we write the Hamiltonian in the form of a 4 x 4 matrix. The eigenvalues (energy levels) are obtained by diagonalizing this 4 x 4 Hamiltonian matrix. Since the Hamiltonian is hermitian, only the lower half of the matrix elements are required to find the eigenvalues. Table I represents the lower half of the Hamiltonian matrix and these matrix

$$\mathcal{H} = W1S_x + W2S_y + W3S_z + W4S_xI_x + W5S_xI_y + W5S_yI_x + W6S_xI_z + W6S_zI_x + W7S_yI_y + W8S_zI_y + W8S_yI_z + W9S_zI_z - g_N\beta_N HI_z \qquad (4\text{-}3)$$

if

$$W1 = \beta H[g_x TG(1,1)TG(1,3) + g_y TG(2,1)TG(2,3) + g_z TG(3,1)TG(3,3)],$$

$$W2 = \beta H[g_x TG(1,2)TG(1,3) + g_y TG(2,2)TG(2,3) + g_z TG(3,2)TG(3,3)],$$

$$W3 = \beta H[g_x TG(1,3)TG(1,3) + g_y TG(2,3)TG(2,3) + g_z TG(3,3)TG(3,3)],$$

$$W4 = h[A_x TH(1,1)TH(1,1) + A_y TH(2,1)TH(2,1) + A_z TH(3,1)TH(3,1)],$$

$$W5 = h[A_x TH(1,2)TH(1,1) + A_y TH(2,2)TH(2,1) + A_z TH(3,2)TH(3,1)],$$

$$W6 = h[A_x TH(1,3)TH(1,1) + A_y TH(2,3)TH(2,1) + A_z TH(3,3)TH(3,1)],$$

$$W7 = h[A_x TH(1,2)TH(1,2) + A_y TH(2,2)TH(2,2) + A_z TH(3,2)TH(3,2)],$$

$$W8 = h[A_x TH(1,2)TH(1,3) + A_y TH(2,2)TH(2,3) + A_z TH(3,2)TH(3,3)],$$

and

$$W9 = h[A_x TH(1,3)TH(1,3) + A_y TH(2,3)TH(2,3) + A_z TH(3,3)TH(3,3)].$$

With the help of raising and lowering operators

$$S_+ = S_x + iS_y, \quad , \quad I_+ = I_x + iI_y,$$

$$S_- = S_x - iS_y \ \text{and} \quad , \quad I_- = I_x - iI_y$$

the Hamiltonian becomes

elements listed in the table are given below:

$A(1,1) = W3/2 + W9/4 - g_n\beta_n H/2$

$A(2,1) = Q4/2$

$A(3,1) = Q1 + Q4/2$

$A(4,1) = Q2$

$A(2,2) = Q3/2 - W9/4 + g_n\beta_n H/2$

$A(3,2) = Q3$

$A(4,2) = -Q4/2$

$A(3,3) = -W3/2 - W9/4 - g_n\beta_n H/2$

$A(4,3) = -Q4/2$

$A(4,4) = -W3/2 + W9/4 + g_n\beta_n H/2$

The energy diagrams for the S = 1/2, I = 1/2 spin system are shown in Figure 10. Figure 10(a) shows the energy level scheme for the case when the hyperfine interaction is greater than the nuclear Zeeman interaction, whereas Figure 10(b) shows the case in which the nuclear Zeeman interaction is greater than the hyperfine interaction.

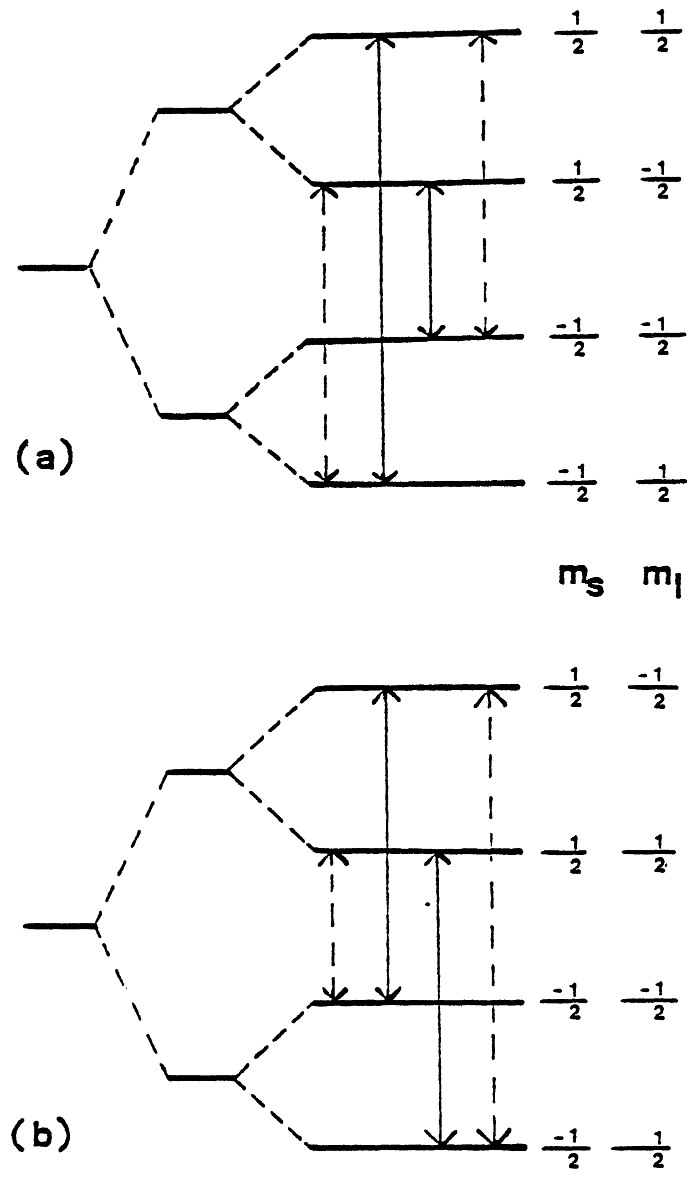

Figure 10. Part (a) shows the energy level scheme for the case when the hyperfine interaction is greater than the nuclear Zeeman interaction and part (b) shows the case when the nuclear Zeeman interaction is greater than the hyperfine interaction

TABLE I

LOWER HALF OF THE SPIN HAMILTONIAN MATRIX FOR AN S=1/2, I=1/2 SPIN SYSTEM

	$\|\frac{1}{2},\frac{1}{2}\rangle$	$\|\frac{1}{2},-\frac{1}{2}\rangle$	$\|-\frac{1}{2},-\frac{1}{2}\rangle$	$\|-\frac{1}{2},\frac{1}{2}\rangle$
$\|\frac{1}{2},\frac{1}{2}\rangle$	A(1,1)			
$\|\frac{1}{2},-\frac{1}{2}\rangle$	A(2,1)	A(2,2)		
$\|-\frac{1}{2},-\frac{1}{2}\rangle$	A(3,1)	A(3,2)	A(3,3)	
$\|-\frac{1}{2},\frac{1}{2}\rangle$	A(4,1)	A(4,2)	A(4,3)	A(4,4)

CHAPTER V

LOW DOSES AND DEFECT PRODUCTION MECHANISMS

Introduction

Result obtained from low-dose radiation tests on quartz resonators have been recently summarized by Norton et al. (48). Of their conclusions, two held implications as to fundamental defect properties within the bulk of the quartz material. These were (1) the lack of correlation between aluminum content and radiation-induced frequency shifts for low-dose levels and (2) the failure to predict the low-level radiation sensitivity of a resonator by extrapolating from the high-level radiation data. By using the electron spin resonance technique, investigations of radiation-induced point defects have been extended to lower dose levels in order to understand the responsible production mechanisms.

In this portion of our study, we have concentrated on the aluminum impurity. We believe that the production of $[AlO_4]^\circ$ centers will correlate with the radiation response of a quartz resonator for two reasons, both of which are related to the acoustic loss spectrum of the resonator. First, formation of $[AlO_4]^\circ$ centers is accompanied by the destruction of $[AlO_4/Na^+]^\circ$ centers. (This latter defect is often referred to as the Al-Na^+ center.) The $[AlO_4/Na^+]^\circ$

center has a very intense acoustic loss peak at low temperature which has been described in considerable detail by King (6) and by Martin (36). Second, the $[AlO_4]^\circ$ center itself has associated acoustic loss peaks (6, 36-37). Radiation-induced changes in these various loss peaks are directly translated into frequency shifts of the resonator.

Table II summarizes the information available about each sample, including aluminum content, growth region, sweeping status, and grower. Of the four Thermodynamic samples involved, two were cut from the z-growth region of the original stone and two were cut from the x-growth region. The six Sawyer samples were z-growth Premium Q material; they were cut from two separate bars (labeled PQI and PQK). Two of the Sawyer samples (PQI7 and PQI8) had been swept in a hydrogen atmosphere at Oklahoma State University by Professor Joel J. Martin. These latter two samples contained significantly more aluminum than the other two samples taken from the same PQI bar. However, the swept and unswept samples were cut from quite different locations in the PQI bar and, presumably, the large differences in aluminum content simply reflect a nonuniform distribution of this impurity within the bar. The determination of aluminum content by ESR method has been described in Chapter I. The defect concentrations were determined by comparison with an $Al_2O_3:Cr^{3+}$ crystal obtained from the National Bureau of Standards.

Aluminum is one of the more pervasive impurities in

TABLE II

DESCRIPTION OF SAMPLES USED IN THIS LOW-DOSE STUDY

SAMPLE	ALUMINUM CONTENT (ppm)	GROWTH REGION	UNSWEPT (U) OR SWEPT (S)	SOURCE
TD5	6.0	z	U	Thermodynamics
TD6	7.5	z	U	
TD7	36.0	x	U	
TD8	36.9	x	U	
PQI4	3.6	z	U	Sawyer
PQI6	4.0	z	U	
PQI7	14.5	z	S	
PQI8	12.4	z	S	
PQK2	8.3	z	U	
PQK4	4.8	z	U	

quartz and also is an important hole trap as discussed in Chapter I. Germanium is another impurity known to be an active charge trapping site in quartz (38,49). However, instead of holes, the germanium ions trap electrons. Figure 11 schematically illustrates three of the more common germanium defect models. The upper diagram represents the neutral substitutional germanium ion and is labeled the $[GeO_4]^0$ center. The defect in the middle diagram is labeled the $[GeO_4]^-$ center and it consists of an extra electron trapped at a substitutional germanium. The lower diagram in Figure 11 has both an alkali interstitial ion, either Li^+ or Na^+, and the extra electron trapped at the substitutional germanium site. The latter defect is labeled the $[GeO_4/M^+]^0$ center. It was earlier thought that commercially available high-quality quartz contained no detectable concentration of germanium; however, the present work has shown that this is not true and there is probably up to 0.1 ppm of germanium in most commercial quartz material. Even though the germanium is present, we note that the aluminum impurity is also present in all quartz and is at least one-to-two orders of magnitude greater in concentration than the germanium.

Our results are in the form of defect production curves. In each case, the sample was subjected to a sequence of irradiations; after exposure to each increment of radiation, the sample was placed in the ESR spectrometer where the defect concentration was monitored. Thus, each of the data points in our production curves represents the

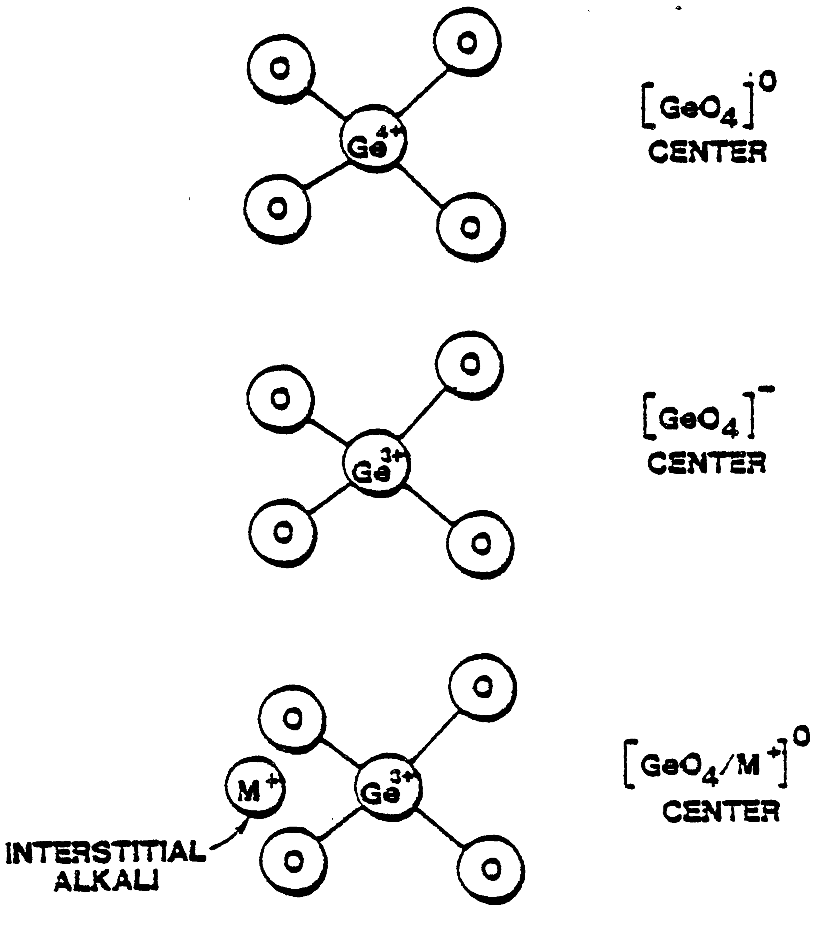

Figure 11. Models of germanium centers

defect concentration resulting from the total dose accumulated at that particular stage in the irradiation sequence. For most samples, this sequential course of events proceeded until saturation of the defect's concentration was observed. When the irradiations were done at 77 K, the sample was not allowed to warm to room temperature until the entire sequence was completed.

Experimental Results

The production of $[AlO_4]^0$ centers at 77 K by ^{60}Co radiation is compared in Figure 12 for four unswept quartz samples. A single saturating exponential provides a good description of the growth curves for the three z-growth samples. This, however, does not appear to describe the x-growth sample. Also, we found that the saturation concentrations of the $[AlO_4]^0$ centers did not scale directly with the known aluminum contents for the three z-growth samples. This lack of correlation with aluminum is even more dramatic when the x-growth sample (TD8) is compared with the z-growth sample (TD6) in the dose range up to 40 krad. Despite having nearly five times more aluminum, the x-growth sample has about half the concentration of $[AlO_4]^0$ centers over this range. Above 40 krad, the $[AlO_4]^0$ center concentration continues to grow for the x-growth sample but remains constant for the z-growth sample. The results presented in Figure 12 suggest that other factors, such as the nature and concentration of unobserved electron traps,

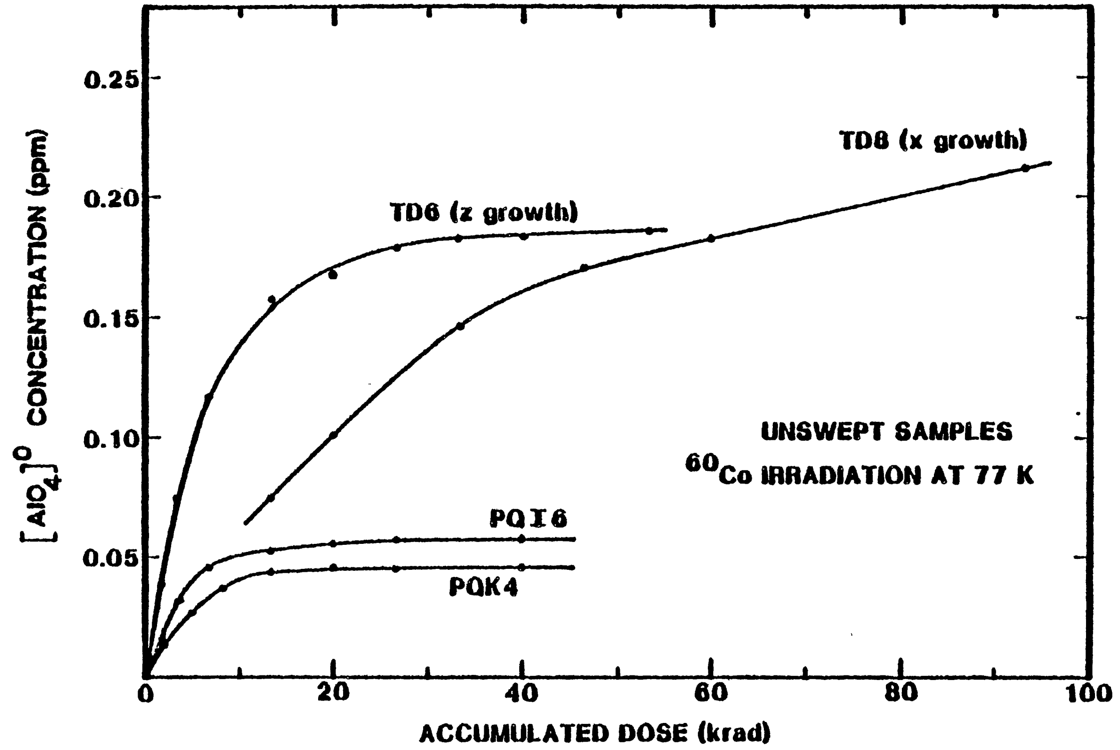

Figure 12. Comparison of defect production at 77 K in four unswept quartz samples

may be as important as the aluminum content in determining the production characteristics of $[AlO_4]^\circ$ centers during 77 K irradiations.

Figure 13 shows the defect production curves for the unswept z-growth sample TD6 as a function of irradiation at 77 K in the ^{60}Co gamma cell. The growth curves for the $[AlO_4]^\circ$ centers and the $[GeO_4]^-$ centers are closely approximated by single saturating exponentials. Both defects saturate at about 30 krad. However, the production of $[AlO_4/Li^+]^+$ centers is quite different. This latter defect exhibits a very rapid growth during the first 3 krad of radiation, then reaches a maximum, and finally drops about 30% to an equilibrium concentration as the radiation accumulates. At the present time, this unique 77 K production behavior of the $[AlO_4/Li^+]^+$ centers is not understood in terms of discreet atomic processes.

Room-Temperature Irradiation

Figure 14 shows the production of $[AlO_4]^\circ$ centers as a function of ^{60}Co irradiation at room temperature. Four unswept samples are compared in this figure; three of these represent z-growth material and one was taken from x-growth material. The $[AlO_4]^\circ$ centers grow rapidly at lower dose in each of the samples, but the final saturation values for the defect concentrations are quite different for the four samples. In contrast to the irradiations at 77 K, described earlier in Figure 12, the room temperature irradiations

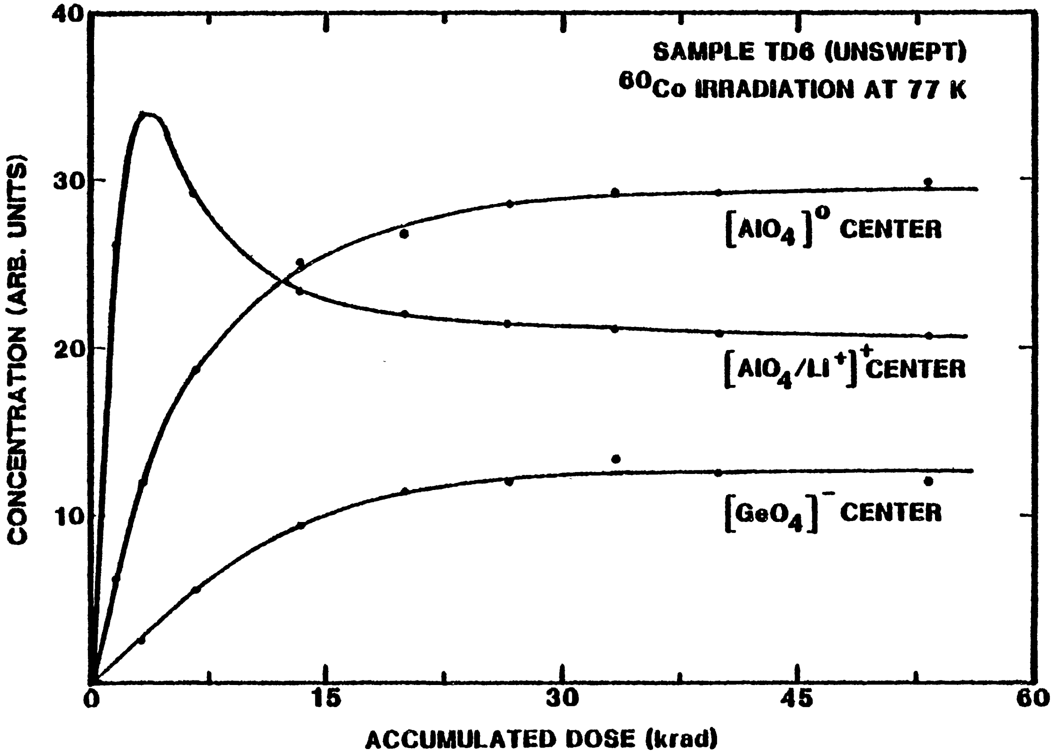

Figure 13. Production of defects in unswept quartz by ^{60}Co radiation at 77 K

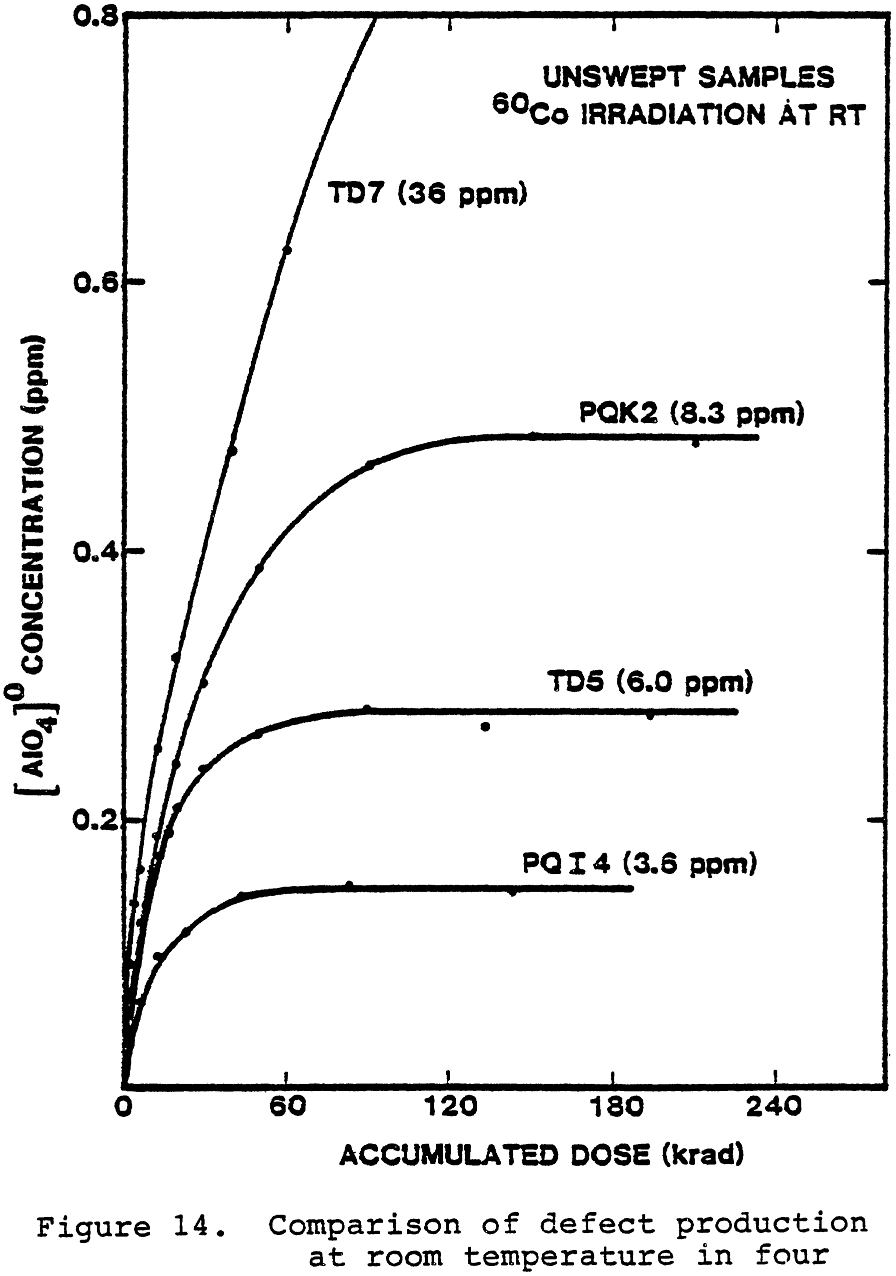

Figure 14. Comparison of defect production at room temperature in four unswept samples

result in a correlation, at least to first order, between the aluminum content of a sample and its saturation concentration of $[AlO_4]^\circ$ centers reached after lengthy irradiation. This is evident from Figure 14 where the aluminum content is included after the sample label for each of the curves.

A surprising result from these room-temperature irradiations was the low values of the saturation concentrations for each of the samples. In the case of the three z-growth samples in Figure 15, 6% or less of the total aluminum content was converted to the $[AlO_4]^\circ$ center form. However, the saturation value of $[AlO_4]^\circ$ centers was between 40% and 70% when high-energy electrons from the Van de Graaff accelerator were used.

Figure 15 is an enlargement of the low-dose portion of Figure 14. This expanded scale provides a more detailed view of the initial growth of the $[AlO_4]^\circ$ centers. Again, we see that the total aluminum content is not a good predictor of the initial radiation sensitivity of a given sample; e.g., sample TD7 has a factor of ten more aluminum than sample PQI4, but the $[AlO_4]^\circ$ centers concentrations for these samples are only a factor of two different during the first 3 krad of accumulated radiation.

A comparison of defect production in swept and unswept samples is presented in Figure 16. Both samples were cut from the same bar and were exposed to ^{60}Co radiation at room temperature. The initial growth rate for the $[AlO_4]^\circ$

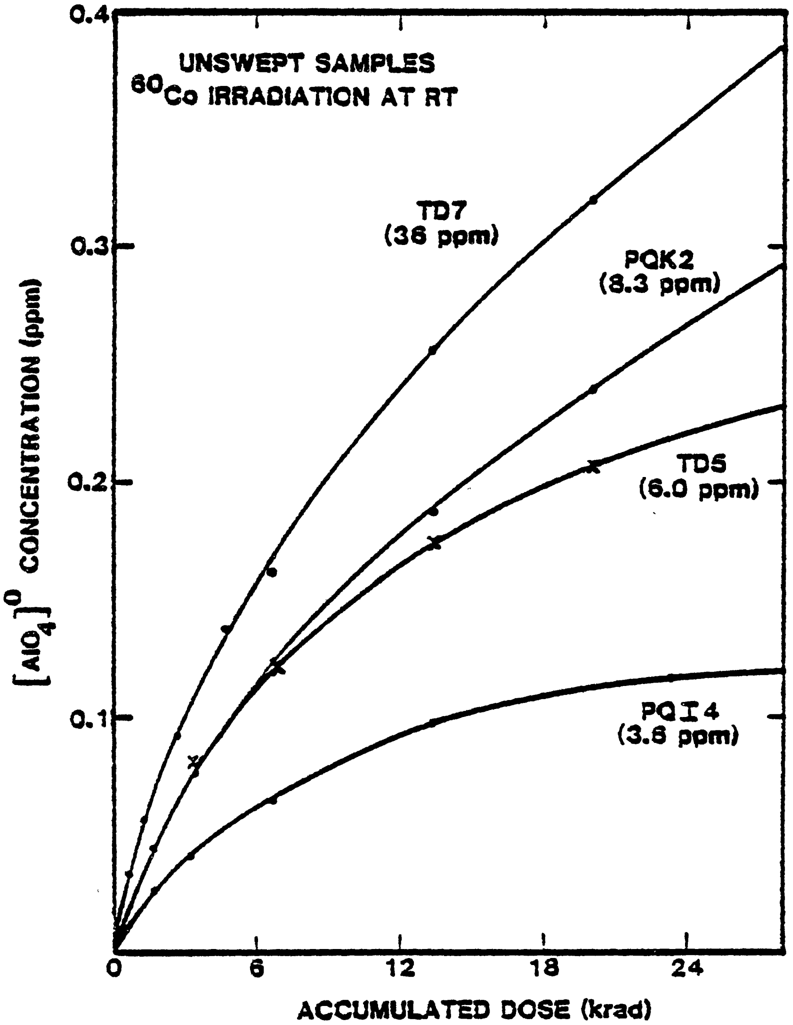

Figure 15. Expanded view of the low-dose data shown in Figure 14

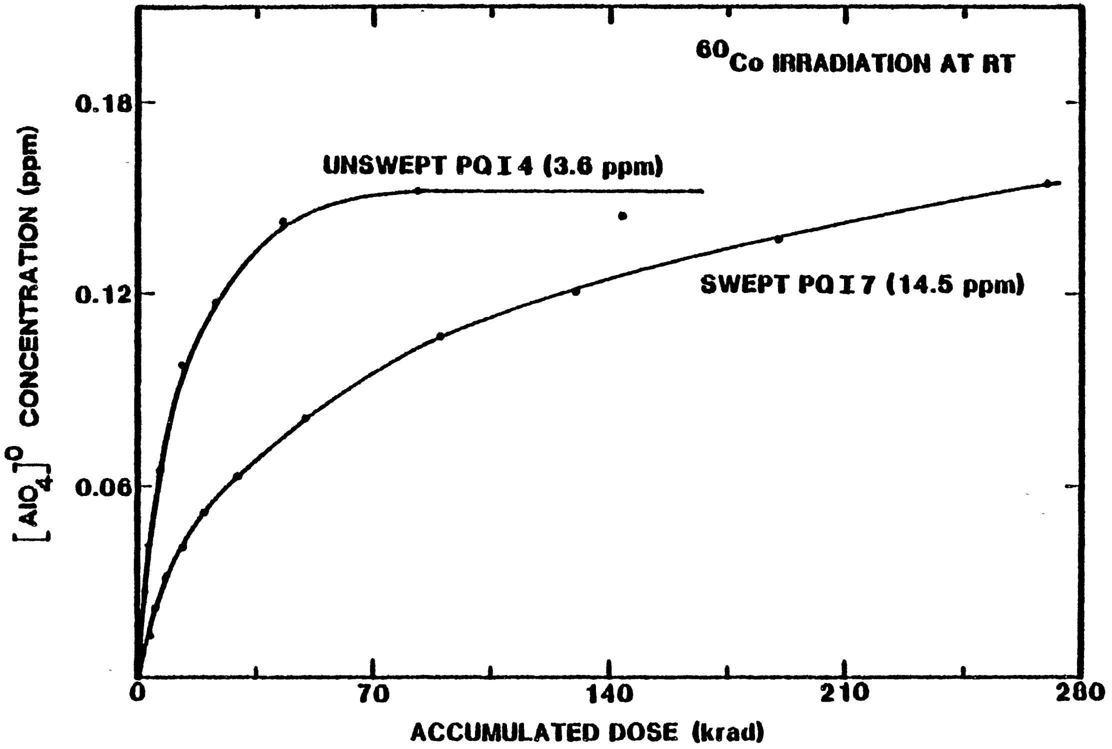

Figure 16. Comparison of defect production at room temperature in a swept and an unswept samples

centers is significantly greater in the unswept sample PQI4 than in the hydrogen-swept sample PQI7. This effect is even more striking when one considers that PQI7 has a factor of four higher aluminum content than PQI4. These results are in agreement with earlier suggestions that interstitial alkali ions can act as electron traps (50).

Radiation Response of Oscillators

It is well known that the formation of $[AlO_4]^\circ$ centers by radiation is directly related to changes in the acoustic loss spectrum of quartz resonators. Thus, the production curves for $[AlO_4]^\circ$ centers that are presented in this study should provide insight to the expected frequency shifts of quartz resonators exposed to low radiation doses. In general, we have found that extreme care must be exercised in predicting the radiation-induced concentrations of $[AlO_4]^\circ$ centers and other defects when the quartz is exposed to low doses. This is especially true for doses below approximately 10 krads. It appears that knowledge of the total aluminum content of a sample is not sufficient information from which to reliably predict the final saturated value of the $[AlO_4]^\circ$ concentrations after irradiation and that other factors such as the nature and concentration of available electron traps are equally important.

Defect Production Mechanisms

The effects of 77 K and room temperature irradiations are compared in Figure 17. The two samples, PQI7 and PQI8, had similar amounts of aluminum and they were both hydrogen swept. The Van de Graaff accelerator was used instead of the ^{60}Co cell in the experiment. The dose rate of the accelerator was approximately 40 rad/sec and the arbitrary dose units in Figure 17 are nearly equal to kilorads. The growth rate for the $[AlO_4]^o$ centers is much less at 77 K than at room temperature, and this suggests that temperature-dependent defect production mechanisms may be involved. Since both of these samples were hydrogen swept, the radiation must lead to the dissociation of hydrogen from aluminum sites in the quartz.

The most interesting of the radiation-related questions in quartz concerns the mechanisms for dissociation of either the alkalis or the protons from the aluminum. Figure 18 provides a schematic representation of the thermal process. The alkali case is considered on the left side of the figure. Initially, the Li^+ and Al^{3+} ions are bound, but isolated, in the lattice. Then, during irradiation, a hole becomes trapped at an oxygen adjacent to the aluminum and forms the $[AlO_4/Li^+]^+$ center, as illustrated at the top left in Figure 18. The middle and lower left portions of Figure 18 show the potential wells for the Li^+ and the hole. We assume the hole is in a deeper well than the alkali. Below 200 K there is insufficient thermal energy for either the

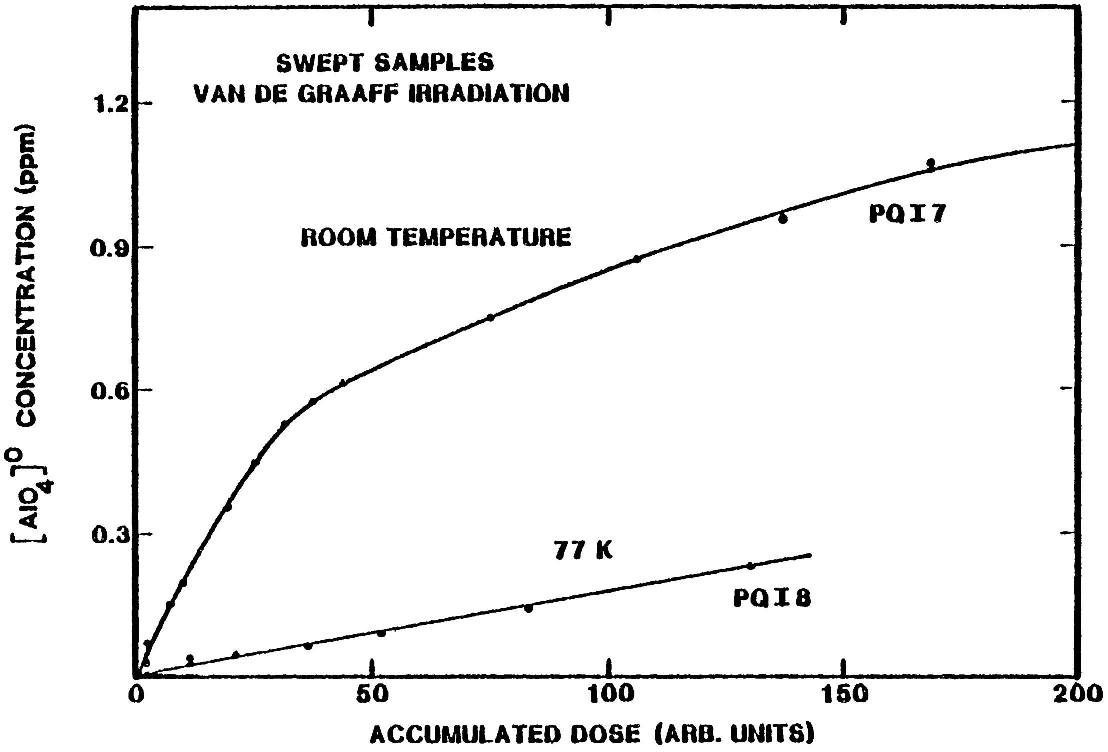

Figure 17. Comparison of defect production at 77 K and room temperature for swept samples

alkali or the hole to escape from their potential wells. At 200 K sufficient thermal energy is available for the alkali, but not the hole, to start escaping. At room temperature, either the alkali or the hole can thermally escape from the aluminum site.

The right side of Figure 18 shows how the hydrogen can escape from the aluminum. As in the case of the alkali, the hydrogen and the aluminum are initially bound, but isolated, in the lattice. Then, radiation forms the $[AlO_4/H^+]^+$ centers, as illustrated at the top right of Figure 18. The potential wells for the proton and the hole are shown in the middle and lower right portions of the figure. Now, we assume that the well for the proton is deeper than that for the hole. At 200 K, there is sufficient thermal energy for the hole to escape from the aluminum, but not the proton. However, at room temperature either the hole or the proton can thermally escape. As the proton thermally diffuses away, we are left with an $[AlO_4]^\circ$ center. It is important to note that this last mechanism is only operative near or above room temperature.

Since the 77 K radiation produced $[AlO_4]^\circ$ centers in the swept sample (see Figure 16), there must be a non-thermal mechanism for dissociating the proton from the aluminum. For this purpose, we propose the process described in Figure 19. Basically, we are starting with the $[AlO_4/H^+]^\circ$ center in line (a). Then, upon irradiation, the $[AlO_4/H^+]^+$ center is formed as in the line (b) of the

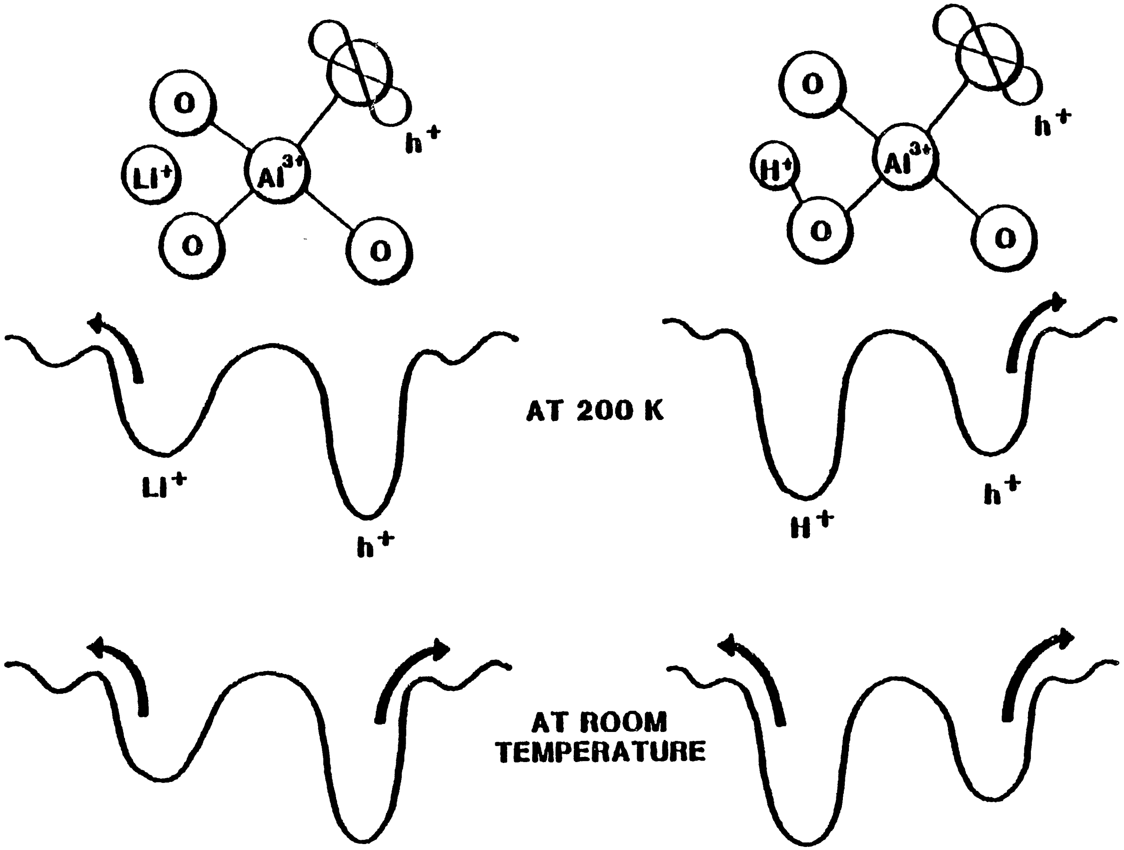

Figure 18. Thermally activated mechanisms for dissociation of alkalis and protons from substitutional aluminum

figure. However, some of the electrons will return to this defect as illustrated in line (c). Most of these returning electron will recombine with the hole and restore the original $[AlO_4/H^+]^\circ$ centers. In some cases, the returning electron will go to the OH^- side of the defect and form an OH^{2-} molecule, as shown in line (d). This OH^{2-} molecule will be very unstable and will immediately dissociate into a hydrogen atom and an oxygen ion as in line (e). The hydrogen atom will thermally diffuse away and the final result will be the $[AlO_4]^\circ$ center, as shown in line (f) of Figure 19.

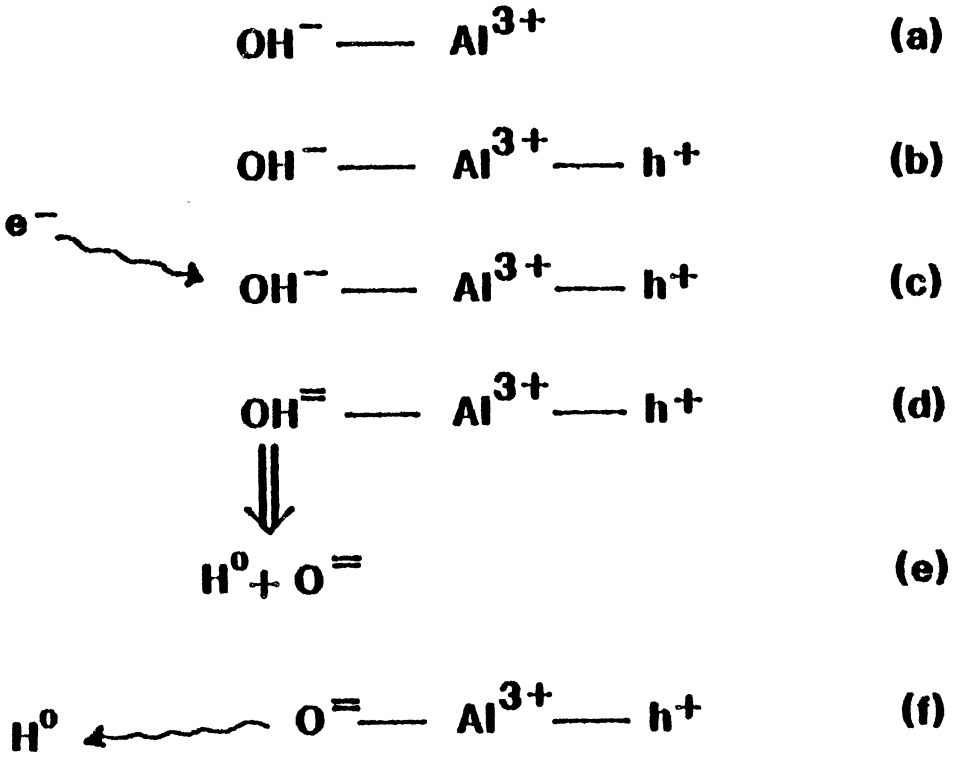

Figure 19. Proposed non-thermally activated process dissociation of protons for aluminum

CHAPTER VI

EXPERIMENTAL RESULTS FOR H CENTERS

ESR Spectra

When synthetic quartz is irradiated at 77 K for extended times, two new centers labeled H-1 and H-2, are created. The ESR spectra taken at 18 K and 37 K for the H-1 and H-2 centers, respectively, are shown in Figure 20. Because of line broadening resulting from relaxation effects, the H-1 centers become undetectable as the temperature rises above 30 K. The H-2 centers become a single line, as shown in Figure 21, when the temperature is 77 K. Both of these centers are a doublet at low temperature when the magnetic field is parallel to the sample's c-axis. Furthermore, each of these doublets splits into three sets of doublets when the magnetic field is rotated away from the crystal's c-axis. The H-1 and H-2 centers are stable as long as the sample is kept at 77 K after the irradiation. Two forbidden transitions, arising from nuclear spin-flips, can be seen on each side of the main doublet. They are 10.35 G apart, which is approximately $2g_N\beta_N H$ for both centers. Also, there are pairs of hyperfine lines due to a ^{29}Si nucleus(I = 1/2, natural abundance 4.7%) on each side of the H-1 and H-2 centers. The separations of

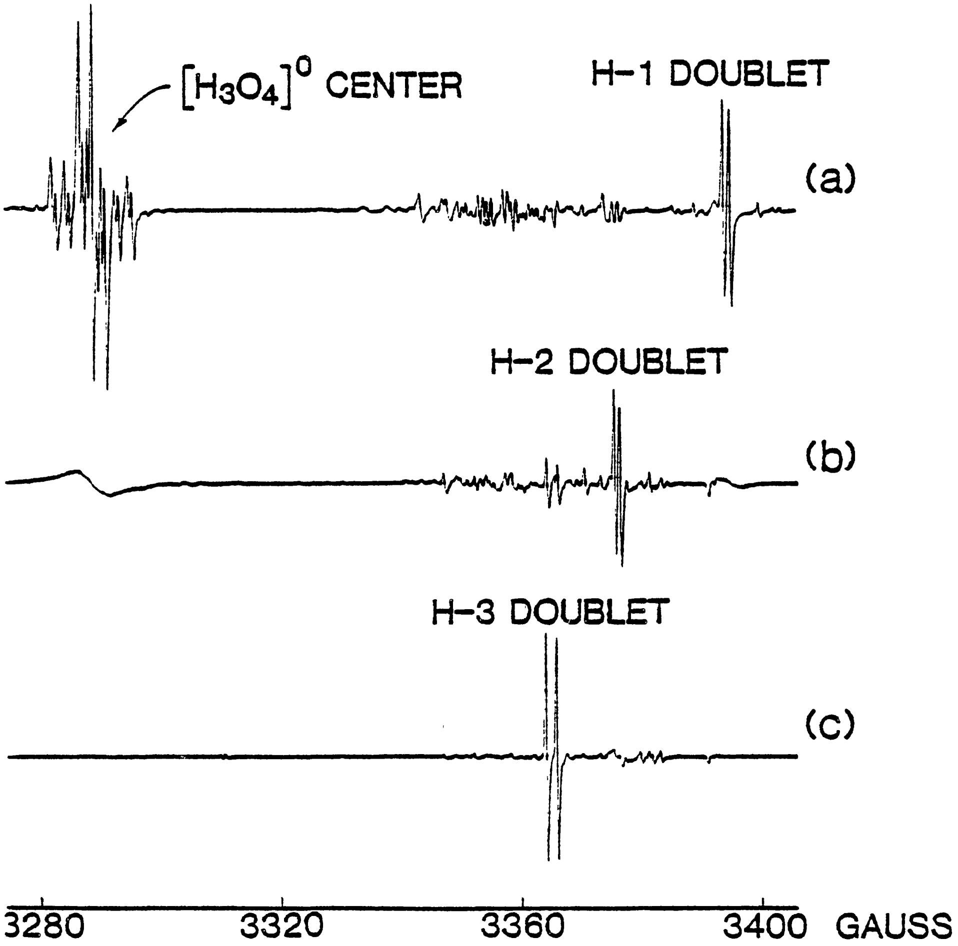

Figure 20. ESR spectra showing the $[H_3O_4]^0$ and the H-1, H-2, and H-3 centers Figures (a), (b), and (c) were taken at 18 K, 37 K, and 57 K, respectively

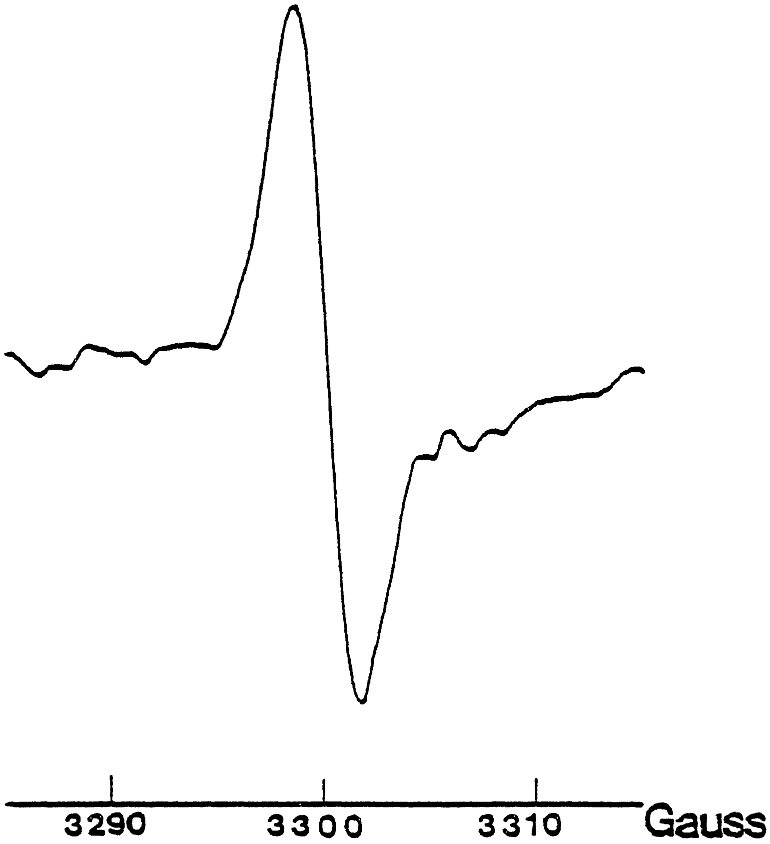

Figure 21. ESR spectrum showing the H-2 centers at 77 K when the magnetic field is along the c-axis. The microwave frequency is 9.283410 GHz

these hyperfine interactions are 16.35 G and 15.45 G for the H-1 and H-2 centers, respectively. The $[H_3O_4]^\circ$ center in part (a) of Figure 20 has been previously reported by Nuttall and Weil (51). They have assigned it to a silicon vacancy containing three protons and having a hole trapped on an adjacent oxygen.

Thermal Behavior

In addition to the H-1, H-2, hydrogen atom (H°), and $[H_3O_4]^\circ$ centers created by irradiation, another center (labeled H-3) appears when the irradiated sample is heated to a temperature higher than 145 K. For this reason, a thermal anneal study was completed in order to better understand the relations between these centers. Before beginning our sequence of anneals, the initial sets of ESR data for the H-1 and H-2 centers were taken at different temperatures (18 K and 37 K, respectively) after 45 minutes of irradiation at 77 K. Then we began to anneal the sample in 15 K steps. The procedure was to hold the sample at a desired temperature for 5 minutes, cool the sample back to 77 K, and then transfer to the microwave cavity without warming. The apparatus for the thermal anneal and liquid helium experiments has been described in Chapter III. With the liquid helium system, ESR data were taken at each of the monitoring temperatures (18, 37, and 57 K) just as was done for the initial set of data taken before beginning the thermal sequence. Only the c-axis spectra were monitored during the thermal anneal study.

Figure 22 shows the ESR thermal anneal results from 77 K to 523 K. We divide the annealing results into three temperature regions, 77 to 140 K, 140 to 300 K, and 300 to 523 K. In the temperature range 100 to 140 K, the H-1 and H-2 centers decrease while the $[H_3O_4]^\circ$ centers increase dramatically. The hydrogen atoms, H°, also decay in this same temperature range, and we believe that this decay is responsible for the growth of the U-2 and U-3 centers discussed in the next chapter. Between 140 K and room temperature, the H-1 and H-2 centers continue to decrease and the $[H_3O_4]^\circ$ centers increase, but at much slower rates. In this latter range, the H-3 centers start to appear at 145 K and they reach their maximum intensity at room temperature. Figure 23 shows the ESR spectrum of the H-3 centers at 77 K (a doublet) and at room temperature (a single line). The H-3 centers was also shown in Figure 20(c) where the measurement temperature was 57 K. The precursor of the H-3 centers is not identified and the connections between the H-1, H-2, $[H_3O_4]^\circ$,and H-3 centers remain vague. However, the possible precursors for the H-3 centers could be the E-type centers (i.e., E_2') as shown in Figure 24. Above room temperature, the H-1 and H-3 centers completely disappear and the $[H_3O_4]^\circ$ centers drop significantly by 400 K. Also, accompanying the H-1 center anneal between 300 and 400 K is an increase in the H-2 centers. The H-2 centers then decrease above 400 K along with the $[H_3O_4]^\circ$

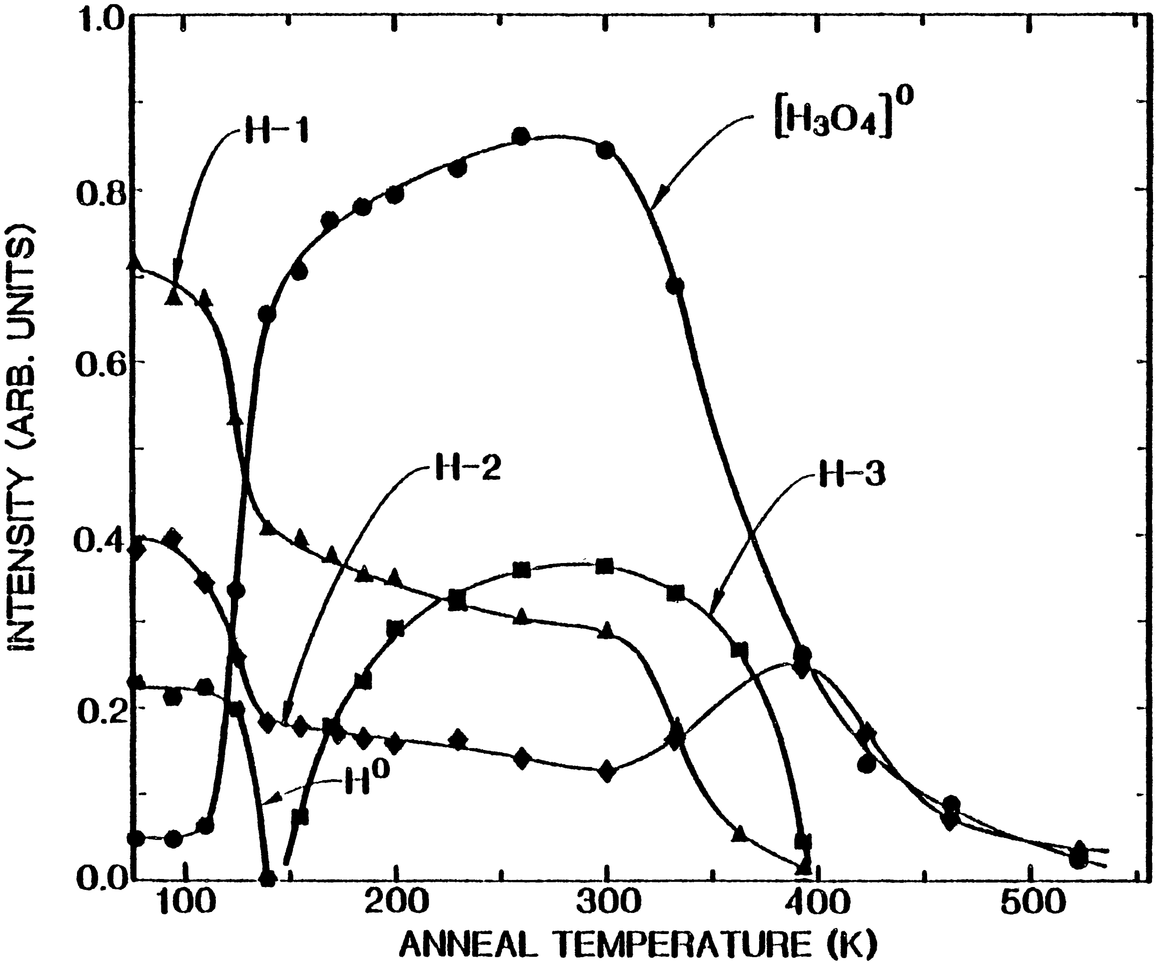

Figure 22. Thermal behavior of the H-1, H-2, H-3, H^0, and $[H_3O_4]^0$ centers. The H-1 and $[H_3O_4]^0$ were monitored at 18 K, the H-2 and H at 37 K, and the H-3 centers at 57 K

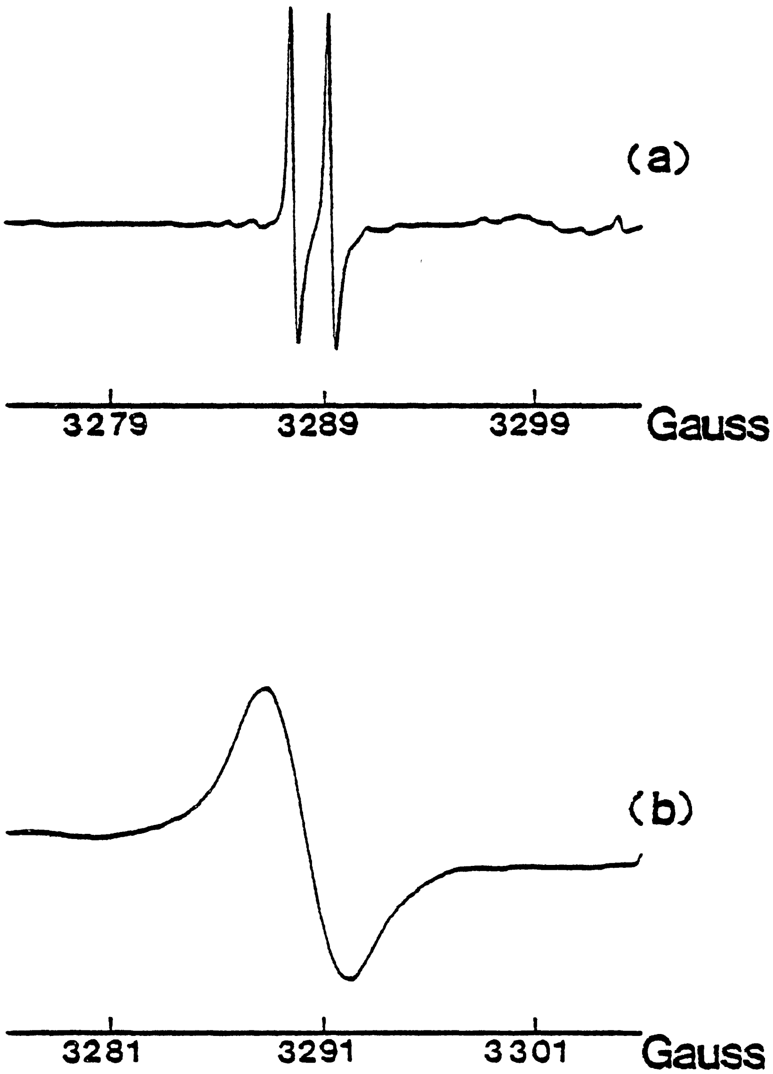

Figure 23. ESR spectra of the H-3 centers at 77 K (a doublet) in trace (a) and at room temperature (a single line) in trace (b) when the magnetic field is along the c-axis. The microwave frequency is 9.287619 GHz

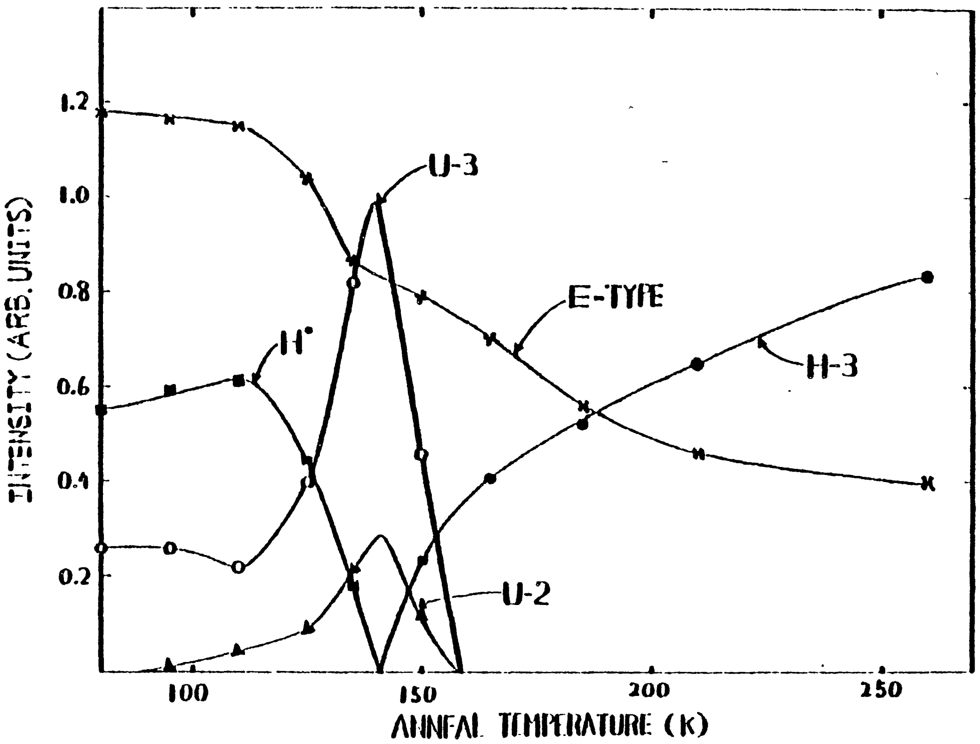

Figure 24. Thermal behavior of the H-3, E-type, H^o, U-2 and U-3 centers. ESR data were taken at 77 K and the sample was held at the desired temperature for five minutes

centers. This suggests an inter-conversion between the H-1 and H-2 centers in this temperature region.

Angular Dependence Study for H-3 Centers

Angular dependence data for the H-3 centers were taken at 77 K (doublets) and at room temperature (single lines). Sample PQI-34 was used and the magnetic field was initially oriented parallel to the crystal's c-axis. The magnetic field was rotated about the X-axis (two-fold crystal axis), and the ESR spectra were recorded at 10° intervals from 0° to +70° and from 0° to -70°. However, due to the limited space within the magnet gap, data beyond +70° and -70° could not be taken without the magnet hitting the cavity. In order to rotate the magnet to ±70°, the two cables (200 gauss rapid scan and the Zeeman field modulation) connected to the front face of the cavity were modified to hang vertically. Also, a complementary set of data for the standard sample $MgO:Cr^{3+}$ was taken immediately after the H-3 data, but with exactly the same configuration. This provided corrections of the magnetic field at each of the different orientations since the gaussmeter probe was not located at the same place as the quartz sample. These field correction factors, determined using the standard sample, are given in Table III and IV for the two sets of H-3 data taken at 77 K and room temperature, respectively.

The principal values and directions of the $\overleftrightarrow{g}$ and $\overleftrightarrow{A}$ matrices can be determined from the angular dependence data.

TABLE III

FIELD-CORRECTION FACTORS AS DETERMINED FROM STANDARD MgO:Cr^{3+} SAMPLE FOR THE H-3 CENTERS AT 77 K (A DOUBLET)

Degrees	($H_{Cr^{3+}}$)	Microwave Frequency (GHz)	ΔH
-70°	3352.708	9.2833726	2.627
-60°	3352.648	9.2833476	2.576
-50°	3352.618	9.2832985	2.564
-40°	3352.612	9.2833184	2.551
-30°	3352.592	9.2833505	2.519
-20°	3352.638	9.2833724	2.557
-10°	3352.686	9.2833231	2.623
0°	3352.648	9.2833294	2.583
+10°	3352.632	9.2830884	2.654
+20°	3352.580	9.2830761	2.606
+30°	3352.536	9.2830660	2.556
+40°	3352.504	9.2830836	2.527
+50°	3352.514	9.2830813	2.538
+60°	3352.534	9.2831001	2.552
+70°	3352.592	9.2831204	2.602

TABLE IV

FIELD-CORRECTION FACTORS AS DETERMINED FROM STANDARD $MgO:Cr^{3+}$ SAMPLE FOR THE H-3 CENTERS AT ROOM-TEMPERATURE (A SINGLE LINE)

Degrees	$(H_{Cr^{3+}})$	Microwave Frequency (GHz)	ΔH
-60°	3352.988	9.2879717	1.248
-50°	3352.998	9.2879942	1.249
-40°	3353.016	9.2880072	1.263
-30°	3353.070	9.2880200	1.312
-20°	3353.106	9.2880389	1.341
-10°	3353.128	9.2880496	1.359
0°	3353.094	9.2880629	1.321
$+10^{\circ}$	3352.572	9.2865654	1.339
$+20^{\circ}$	3352.564	9.2865593	1.333
$+30^{\circ}$	3352.510	9.2865536	1.281
$+40^{\circ}$	3352.490	9.2865500	1.263
$+50^{\circ}$	3352.488	9.2865399	1.264
$+60^{\circ}$	3352.512	9.2865345	1.290

Two computer programs were utilized to obtain the best sets of parameters for the $\overleftrightarrow{g}$ and $\overleftrightarrow{A}$ matrices. The first program predicts the ESR line positions for different orientations of the magnetic field when given a set of spin Hamiltonian parameters and a microwave frequency. The second program calculates the final set of parameters when the experimental microwave frequencies and ESR line positions are provided as input data. The details of these two programs can be found in reference (22).

Table V and VI list the measured magnetic field values (both uncorrected and corrected), the calculated magnetic field values, and the measured microwave frequencies for the H-3 centers at 77 K and at room temperature, respectively. Table VII and VIII contain the final sets of parameters which were determined by the fitting program. From each final set of parameters, the angular dependence of the corresponding ESR spectra can be predicted by the line position program. Figure 25 and 26 show these computer predicted angular dependent spectra for the H-3 center at 77 K and at room temperature, respectively.

Angular Dependent Study for H-2 Centers

Because of line broadening from spin lattice relaxation effects, the H-2 centers appear as a single line at 77 K when the magnetic field is parallel to the crystal's c-axis. Angular dependence data were taken in the same fasion as for the H-3 centers. The measured magnetic field values (both

TABLE V

ANGULAR DEPENDENT DATA FOR THE H-3 CENTERS AT 77 K

Angle	Uncorrected Field in Gauss	Corrected Field in Gauss	Calculated Field in Gauss	Microwave Frequency in GHz
-70°	3311.374	3308.779	3308.944	9.2817298
	3311.374	3308.779	3308.670	9.2817298
	3293.550	3292.968	3293.156	9.2817035
	3298.288	3295.704	3295.947	9.2817045
	3230.168	3227.637	3228.163	9.2815999
	3229.502	3226.971	3227.499	9.2816174
-60°	3313.964	3311.418	3311.399	9.2816592
	3313.434	3310.888	3310.960	9.2816505
	3302.232	3299.695	3299.726	9.2816642
	3304.166	3301.627	3301.709	9.2816558
	3227.436	3224.956	3225.487	9.2816576
	3226.676	3224.197	3224.714	9.2816484
-50°	3314.406	3311.870	3311.795	9.2816374
	3313.684	3311.150	3311.122	9.2816358
	3306.926	3304.937	3304.353	9.2816302
	3307.976	3305.446	3305.416	9.2816375
	3229.728	3327.258	3227.853	9.2816359
	3228.802	3326.333	3226.921	9.2816373
-40°	3312.694	3310.174	3310.084	9.2816103
	3311.732	3309.212	3309.135	9.2816032
	3309.114	3306.596	3306.460	9.2816032
	3309.114	3306.596	3306.589	9.2816032
	3236.846	3234.383	3235.009	9.2815888
	3235.740	3233.278	3233.884	9.2815945
-30°	3309.102	3306.616	3306.481	9.2816688
	3307.786	3305.301	3305.247	9.2816552
	3308.428	3305.942	3305.790	9.2816649
	3307.786	3305.301	3305.070	9.2816552
	3248.022	3245.581	3246.175	9.2816597
	3246.688	3244.248	3244.843	9.2816547
-20°	3303.954	3301.434	3301.437	9.2816581
	3302.524	3300.005	3299.944	9.2816557
	3305.036	3302.515	3301.048	9.2816530
	3303.954	3301.434	3301.437	9.2816581
	3261.984	3259.496	3260.104	9.2816700
	3260.470	3257.983	3258.573	9.2816693

TABLE V (continued)

Angle	Uncorrected Field in Gauss	Corrected Field in Gauss	Calculated Field in Gauss	Microwave Frequency in GHz
-10°	3298.022	3295.442	3295.574	9.2815363
	3296.332	3293.753	3293.883	9.2815253
	3299.270	3296.689	3296.804	9.2815417
	3297.496	3294.916	3295.574	9.2815314
	3277.169	3274.605	3275.185	9.2815545
	3275.507	3272.944	3273.490	9.2815225
0°	3291.917	3289.381	3289.606	9.2815066
	3290.142	3287.607	3287.801	9.2815044
+10°	3286.548	3283.947	3284.247	9.2815905
	3284.772	3282.172	3282.429	9.2815925
	3283.954	3281.355	3281.725	9.2815702
	3282.468	3279.870	3280.227	9.2815876
	3304.202	3301.587	3301.564	9.2815910
	3302.390	3299.776	3299.724	9.2815830
+20°	3282.436	3279.884	3280.132	9.2815941
	3280.716	3278.166	3278.399	9.2816187
	3276.312	3273.765	3274.125	9.2815972
	3275.412	3272.866	3273.218	9.2816040
	3312.170	3309.595	3309.513	9.2816100
	3310.420	3307.847	3307.719	9.2816178
+30°	3280.032	3277.532	3277.740	9.2815973
	3278.484	3275.985	3276.181	9.2816026
	3269.812	3267.319	3267.717	9.2815943
	3269.812	3267.319	3267.594	9.2815943
	3315.038	3312.511	3312.401	9.2816094
	3313.402	3310.876	3310.728	9.2815978
+40°	3279.692	3277.219	3277.351	9.2816404
	3278.354	3275.882	3276.029	9.2816178
	3265.424	3262.962	3263.246	9.2816128
	3266.182	3263.720	3264.009	9.2816036
	3312.400	3309.903	3309.840	9.2816329
	3310.642	3308.446	3308.347	9.2816464
+50°	3281.368	3278.884	3279.009	9.2816266
	3280.338	3277.854	3277.960	9.2816259
	3263.430	3260.959	3261.217	9.2816163
	3265.082	3262.610	3262.882	9.2816259
	3304.606	3302.104	3302.176	9.2816033
	3303.342	3300.845	3300.895	9.2816232

TABLE V (continued)

Angle	Uncorrected Field in Gauss	Corrected Field in Gauss	Calculated Field in Gauss	Microwave Frequency in GHz
+60°	3284.916	3282.416	3282.524	9.2816354
	3284.126	3281.627	3281.751	9.2816350
	3264.110	3261.626	3261.853	9.2816384
	3266.560	3264.074	3264.351	9.2816517
	3292.702	3290.196	3290.425	9.2816419
	3291.644	3289.139	3289.360	9.2816326
+70°	3289.926	3287.373	3287.486	9.2816509
	3289.362	3286.809	3286.961	9.2816629
	3267.404	3264.868	3265.078	9.2816660
	3270.516	3267.978	3268.252	9.2816642
	3278.232	3275.688	3276.108	9.2816544
	3277.386	3274.842	3275.236	9.2816731

TABLE VI

ANGULAR DEPENDENT DATA FOR THE H-3 CENTERS AT ROOM-TEMPERATURE

Angle	Uncorrected Field in Gauss	Corrected Field in Gauss	Calculated Field in Gauss	Microwave Frequency in GHz
-60°	3305.942	3304.712	3305.372	9.2851380
	3305.942	3304.712	3303.398	9.2851380
	3231.492	3230.290	3230.561	9.2851387
-50°	3307.751	3306.751	3307.075	9.2851340
	3307.984	3306.751	3306.606	9.2851340
	3234.550	3233.345	3233.410	9.2851344
-40°	3308.462	3307.216	3306.908	9.2851280
	3308.462	3307.216	3307.601	9.2851280
	3241.894	3240.673	3240.588	9.2851339
-30°	3306.938	3305.644	3304.890	9.2851340
	3306.938	3305.644	3306.257	9.2851340
	3252.780	3251.507	3251.305	9.2851342
-20°	3303.238	3301.917	3301.276	9.2851317
	3303.238	3301.917	3302.744	9.2851317
	3265.982	3264.676	3264.350	9.2851322
-10°	3298.164	3296.827	3296.513	9.2851366
	3298.164	3296.827	3297.504	9.2851366
	3279.840	3278.510	3278.203	9.2851590
0°	3292.498	3291.201	3291.188	9.2851406
+10°	3286.226	3284.914	3285.945	9.2845500
	3286.226	3284.914	3284.569	9.2845500
	3302.518	3301.199	3301.680	9.2845528
+20°	3282.491	3281.186	3281.412	9.2845582
	3279.881	3278.577	3278.446	9.2845559
	3309.348	3308.032	3308.325	9.2845579
+30°	3279.396	3276.390	3278.124	9.2845729
	3274.494	3270.060	3273.541	9.2845717
	3311.258	3306.996	3310.247	9.2845687
+40°	3277.624	3276.390	3276.466	9.2845729
	3271.292	3270.060	3270.429	9.2845717
	3308.242	3306.996	3307.190	9.2845739

TABLE VI (continued)

Angle	Uncorrected Field in Gauss	Corrected Field in Gauss	Calculated Field in Gauss	Microwave Frequency in GHz
+50°	3277.858	3276.622	3276.629	9.2845781
	3270.100	3268.867	3269.467	9.2845754
	3300.718	3299.473	3299.561	9.2845776
+60°	3279.784	3278.522	3278.595	9.2845818
	3271.324	3270.065	3270.767	9.2845798
	3289.504	3288.238	3288.362	9.2845822

TABLE VII

SPIN-HAMILTONIAN PARAMETERS FOR THE H-3 CENTERS AS DETERMINED AT 77 K

		θ	ϕ
g_x	2.00706	66.2	294.4
g_y	2.00169	140.1	352.5
g_z	2.05716	60.1	39.1
A_x	5.08	106.7	181.8
A_y	-10.30	93.5	272.8
A_z	5.05	17.1	194.3

TABLE VIII

SPIN-HAMILTONIAN PARAMETERS FOR THE H-3 CENTERS AS DETERMINED AT ROOM-TEMPERATURE

		θ	ϕ
g_x	2.00859	92.2	297.4
g_y	2.00409	151.1	31.4
g_z	2.05371	61.2	26.2

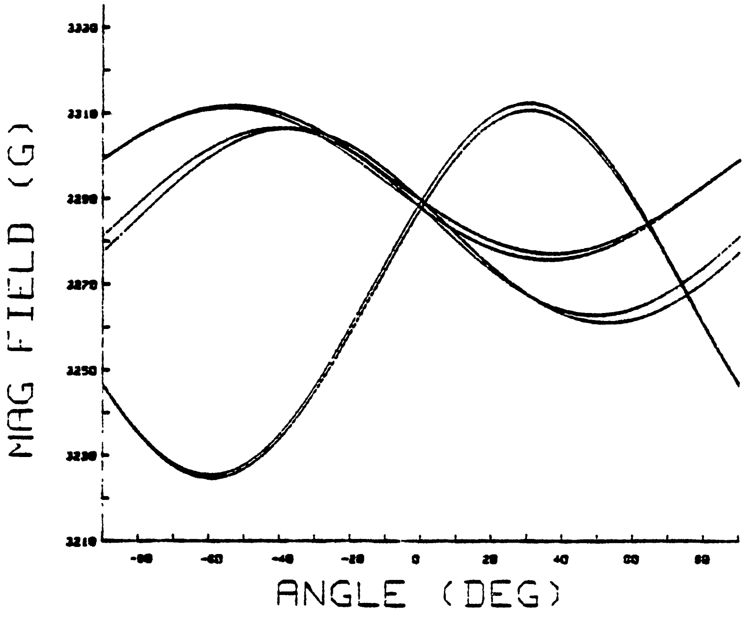

Figure 25. Computer predicted angular dependence for the H-3 centers at 77 K

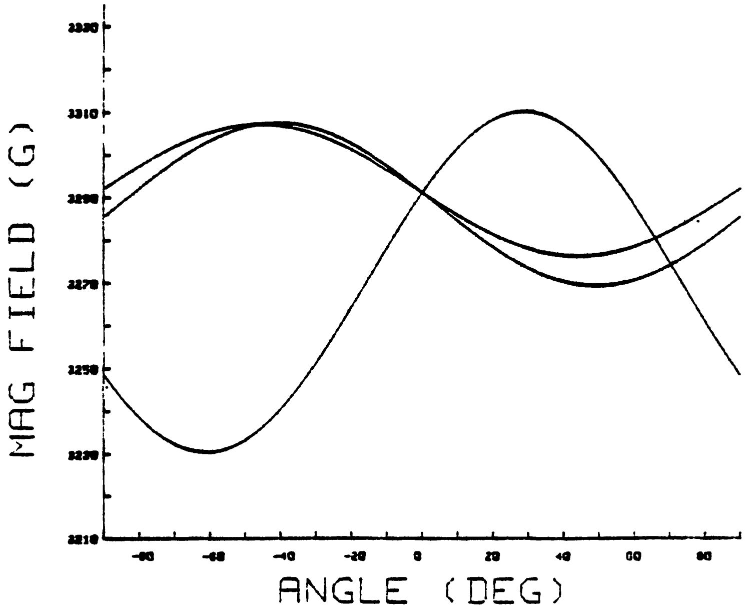

Figure 26. Computer predicted angular dependence for the H-3 centers at room temperature

uncorrected and corrected), and the calculated magnetic field values, and the microwave frequencies are given in Table IX. Table X lists the corrected magnetic field values and the field correction factors from the standard sample, $MgO:Cr^{3+}$. Using the line position and fitting programs previously described, the final set of the parameters given in Table XI were determined. The computer predicted angular dependence of the H-2 center is shown in Figure 27.

Discussion

H-1 and H-2 Centers

The goal of our investigation is to determine the appropriate model for each of the observed defects. In the case of the H-1 and H-2 centers there are a number of experimental results which help to narrow our choices to only a few. Thus, models for the H-1 and H-2 centers must be consistent with the following observations: (1) their production curves do not saturate until very high doses of radiation (greater than 100 Megarads), (2) they are holelike because of their positive g shifts, (3) thay contain a single proton as suggested by the doublets in their ESR spectra and by the spin-flip transitions, and (4) their short spin-lattice relaxation times indicate rapid reorientations of holes or ions within the defects.

One of the few defects that can trap simultaneously a hole and a proton is a silicon-oxygen divacancy. Such a defect would have an effective double negative charge and

TABLE IX

ANGULAR DEPENDENT DATA FOR THE H-2 CENTERS AT ROOM-TEMPERATURE

Angle	Uncorrected Field in Gauss	Corrected Field in Gauss	Calculated Field in Gauss	Microwave Frequency in GHz
-70°	3306.676	3304.722	3304.556	9.2814972
	3227.990	3226.083	3225.855	9.2815083
	3154.100	3152.237	3152.045	9.2815085
-60°	3304.914	3302.979	3302.605	9.2818907
	3254.478	3252.573	3252.322	9.2819523
	3161.518	3159.667	3159.442	9.2815374
-50°	3303.168	3301.246	3300.786	9.2818533
	3280.066	3278.158	3299.101	9.2818580
	3177.444	3175.595	3175.185	9.2818776
-40°	3301.556	3299.638	3299.317	9.2818429
	3301.556	3299.638	3299.101	9.2818429
	3200.062	3198.203	3197.699	9.2818490
-30°	3300.740	3298.779	3298.374	9.2817960
	3315.350	3313.381	3313.254	9.2817985
	3226.998	3225.081	3224.595	9.2817899
-20°	3300.486	3298.464	3298.070	9.2817234
	3320.280	3318.246	3318.275	9.2817260
	3255.238	3253.244	3252.817	9.2817248
-10°	3300.520	3298.459	3298.439	9.2816690
	3315.370	3313.300	3313.436	9.2816775
	3281.294	3279.245	3278.909	9.2816640
0°	3301.389	3299.353	3299.440	9.2816269
+10°	3302.909	3300.772	3300.951	9.2817157
	3279.846	3277.724	3278.274	9.2816994
	3313.881	3311.737	3311.550	9.2817193
+20°	3304.674	3302.596	3302.793	9.2817272
	3254.386	3252.339	3252.819	9.2817264
	3315.930	3313.845	3313.483	9.2817167
+30°	3306.863	3304.807	3304.745	9.2817487
	3227.940	3225.933	3226.341	9.2817395
	3306.863	3304.807	3304.954	9.2817487

TABLE IX (continued)

Angle	Uncorrected Field in Gauss	Corrected Field in Gauss	Calculated Field in Gauss	Microwave Frequency in GHz
+40°	3308.376	3306.357	3306.571	9.2814903
	3203.519	3201.564	3202.011	9.2814970
	3289.158	3287.151	3287.211	9.2814781
+50°	3309.848	3307.847	3308.049	9.2814983
	3184.130	3182.205	3182.549	9.2814948
	3264.366	3262.393	3262.768	9.2815054
+60°	3310.572	3308.582	3309.000	9.2815194
	3171.689	3169.782	3169.999	9.2815207
	3236.392	3234.447	3234.913	9.2815141
+70°	3310.896	3308.860	3309.308	9.2815557
	3167.521	3165.573	3165.620	9.2815694
	3208.672	3206.699	3207.151	9.2815696

TABLE X

FIELD-CORRECTION FACTORS AS DETERMINED FROM STANDARD MgO:C_r^{3+} SAMPLE FOR THE H-2 CENTERS AT 77 K

Degrees	($H_{Cr^{3+}}$)	Microwave Frequency (GHz)	ΔH
-70^0	3352.512	9.2846208	1.981
-60^0	3352.486	9.2845993	1.962
-50^0	3352.468	9.2845829	1.950
-40^0	3353.472	9.2846026	1.947
-30^0	3353.514	9.2845969	1.991
-20^0	3353.582	9.2846128	2.054
-10^0	3353.620	9.2846071	2.094
0^0	3353.202	9.2833107	2.144
$+10^0$	3352.222	9.2832954	2.169
$+20^0$	3352.174	9.2833313	2.108
$+30^0$	3352.136	9.2832924	2.084
$+40^0$	3352.096	9.2832883	2.046
$+50^0$	3352.078	9.2832919	2.026
$+60^0$	3352.066	9.2832899	2.015
$+70^0$	3352.096	9.2832438	2.062

TABLE XI

SPIN-HAMILTONIAN PARAMETERS FOR THE H-2 CENTERS AS DETERMINED AT 77 K

		θ	ϕ
g_x	2.00685	119.7	336.5
g_y	1.99733	145.5	122.3
g_z	2.12736	73.9	57.1

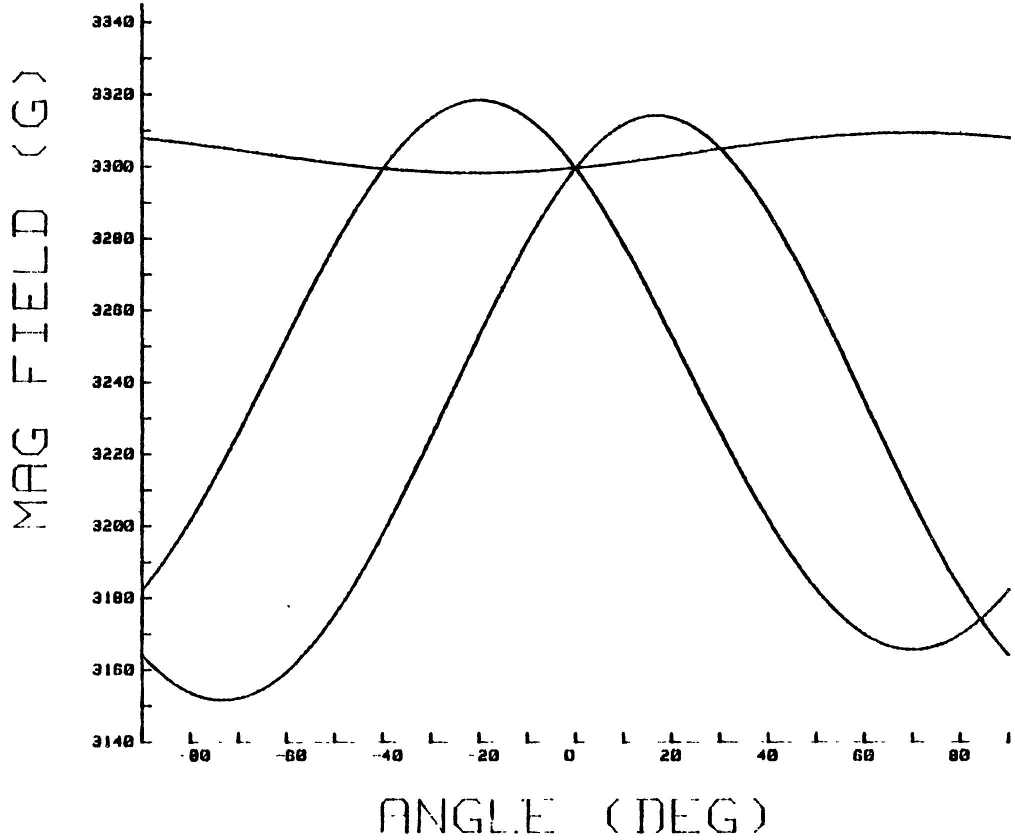

Figure 27. Computer predicted angular dependence for the H-2 centers at room temperature

thus needs two additional positive charges to maintain neutrality. These two additional charges could be two protons, two holes on adjacent oxygen ions, or one proton and one hole. Based on this concept, we offer the following models for the H-1 and H-2 centers. Initially, as shown in Figure 28(a), silicon-oxygen divacancies formed during crystal growth will have two adjacent protons. Subsequent irradiation at 77 K will remove one of the protons and leave one hole and one proton at the divacancy, as shown in Figure 28(b). This gives the H-1 and H-2 centers. The hole would be trapped on a long-bond oxygen for one of the centers and on a short-bond oxygen for the other center.

As the temperature is increased during the thermal anneals, we first reach the region between 100 and 140 K where the H-1 and H-2 centers both undergo significant decay steps. We suggest that this step corresponds to the release of hydrogen atoms from elsewhere in the crystal and their migration to the H-1 and H-2 centers. When the hydrogen atoms combine with the H-1 and H-2 centers, the silicon-oxygen divacancies are converted back to their original forms (i.e., a neutral divacancy with two adjacent protons). The next temperature region of interest occurs between 300 and 400 K. Here the H-1 center decays while the H-2 center grows. We suggest that this behavior results from the jumping of the hole from one type of oxygen to the other. For example, below 300 K, the hole can jump between short-bond oxygens or between long-bond oxygens, but above

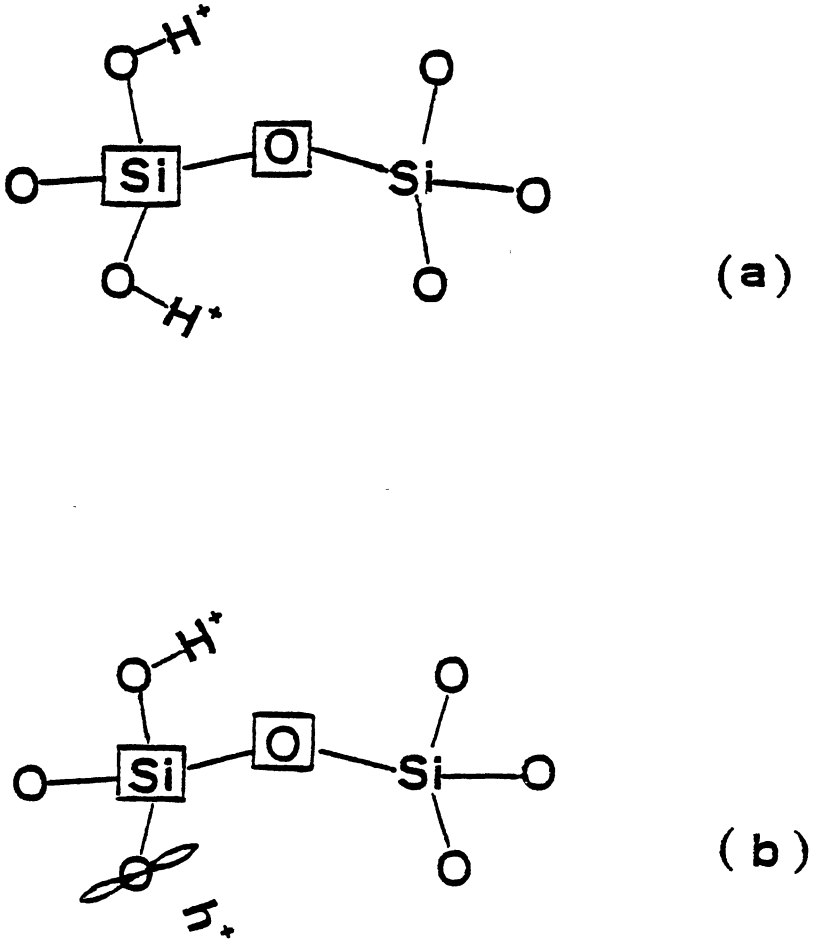

Figure 28. Part (a) shows the divacancy with two protons adjacent to two oxygen ions
Part (b) shows the model for the H-1 and H-2 centers; one proton is replaced by a hole after lengthy 77 K irradiations

300 K, the hole can jump from short to long or vice-versa. One of the two types of oxygen bond lengths will be a deeper trap than the other, and our models would require the hole to be in the deeper potential well in the case of the H-2 center.

It must be emphasized that these suggested models have not been proven. Further analysis of the angular dependence data presented in this chapter will help to prove or disprove them.

H-3 Center

It has proven to be much more difficult to suggest a plausible model for the H-3 center. Nearly all of its characteristics are similar to those of the H-1 and H-2 centers except for two. The H-3 center is holelike and contains a proton. It also exhibits motional broadening between 77 K and room temperature. However, unlike the H-1 and H-2 centers, it does not show a hyperfine interaction with a single neighboring silicon nucleus and, most importantly, it is not produced directly by a 77 K irradiation. The H-3 center does not appear after a long irradiation until the sample has been warmed to approximately 145 K. We initially thought that the H-3 center was also a silicon-oxygen divacancy, but this does not seem to agree with the observed production behavior. Thus we leave as an open question the details of the model for the H-3 center.

CHAPTER VII

EXPERIMENTAL RESULTS FOR THE U-CENTERS

As shown in Figure 29, another two hydrogen-related centers, labeled U-2 and U-3, are created when a quartz crystal is irradiated at 77 K. The U-2 and U-3 centers were first reported by Markes and Halliburton (35) in 1979. At that time it was suggested that these defects were oxygen vacancies (because of their long spin-lattices relaxation times) and that they had an adjacent proton (because of their doublet nature). The growth of these centers at the same time hydrogen atoms thermal anneal also supported the hydrogen assignment. The U-2 and U-3 centers exhibit hyperfine splittings of 5.7 and 13.6 G, respectively, when their spectra are taken at 77 K with the magnetic field parallel to the crystal's c-axis and the ESR spectrometer turned out-of-phase. This out-of-phase condition is common for many of the electronlike paramagnetic centers in quartz which have long spin-lattice relaxation times. In addition to the primary doublets, the U-2 and U-3 centers exhibit one set of hyperfine interactions due to a ^{29}Si (I = 1/2, natural abundance 4.7%) nucleus. The separation of this pair of hyperfine lines is 446 G and 482 G for U-2 and U-3 centers, respectively, when the magnetic field is parallel

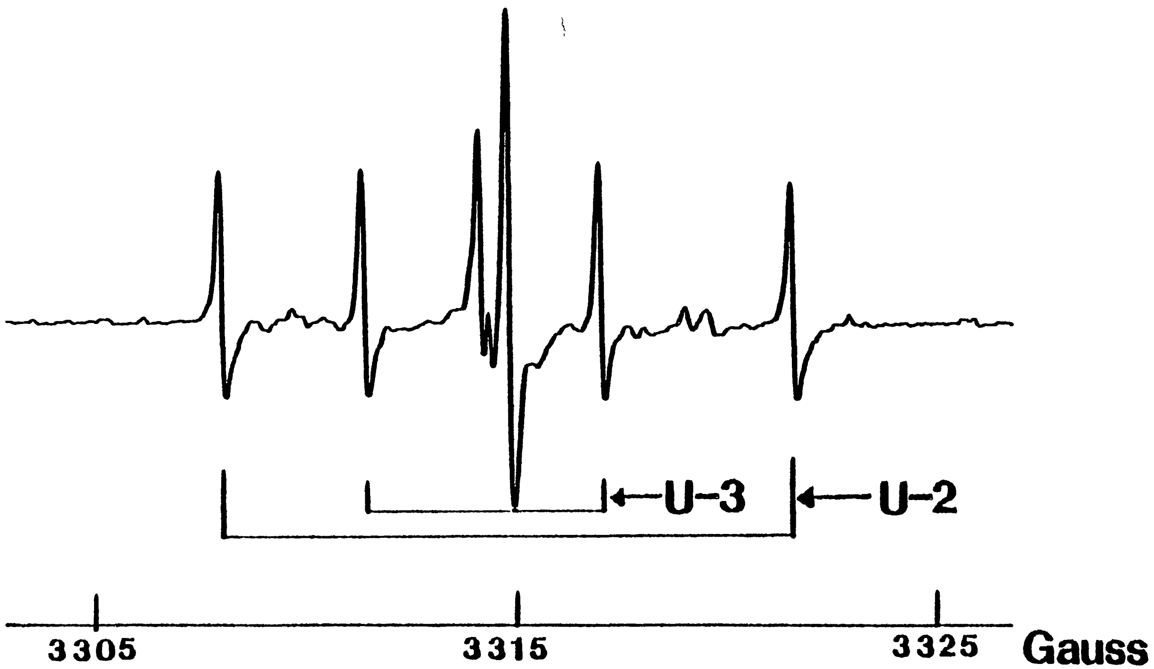

Figure 29. ESR spectra of the U-2 and U-3 centers when the magnetic field is along the c-axis
The microwave frequency is 9.281864 GHz

to the crystal's c-axis. These two centers can be easily bleached by ultraviolet light and both anneal by 160 K.

Thermal Study

The sample used in this study was PQI-21 and the procedures for thermal anneal are the same as described earlier. Figure 30 shows the thermal behavior of the U-2, U-3, and hydrogen atoms during a series of five-minute pulse anneals. Between 90 K and 110 K, the hydrogen atoms and the U-3 centers grow and the U-2 centers decrease. In the range of 110 K to 140 K, the U-2 and U-3 centers both grow while the hydrogen atoms decay. These changes are due to conversions between the hydrogen atoms and the U-centers and this provides some of the evidence to prove that the U-centers are hydrogen-related.

However, if the sample was kept in liquid nitrogen for long periods of time (i.e., 2 weeks after irradiation), we found that the U-2 centers disappeared and the hydrogen atoms and U-3 centers increased by approximately 60% and 40%, respectively. The ESR spectrum of the U-3 centers, with the U-2 centers eliminated, is shown in Figure 31. Also, a thermal anneal study was done for a sample which had been kept in the liquid nitrogen for two weeks after a 77 K irradiation. The thermal stability of the U-2, U-3, H°, and E- type centers (i.e., E_2') was shown in Figure 24 after a series of five-minute pulse anneals. Between 90 K and 110 K, the hydrogen atoms and U-2 centers (they were not present

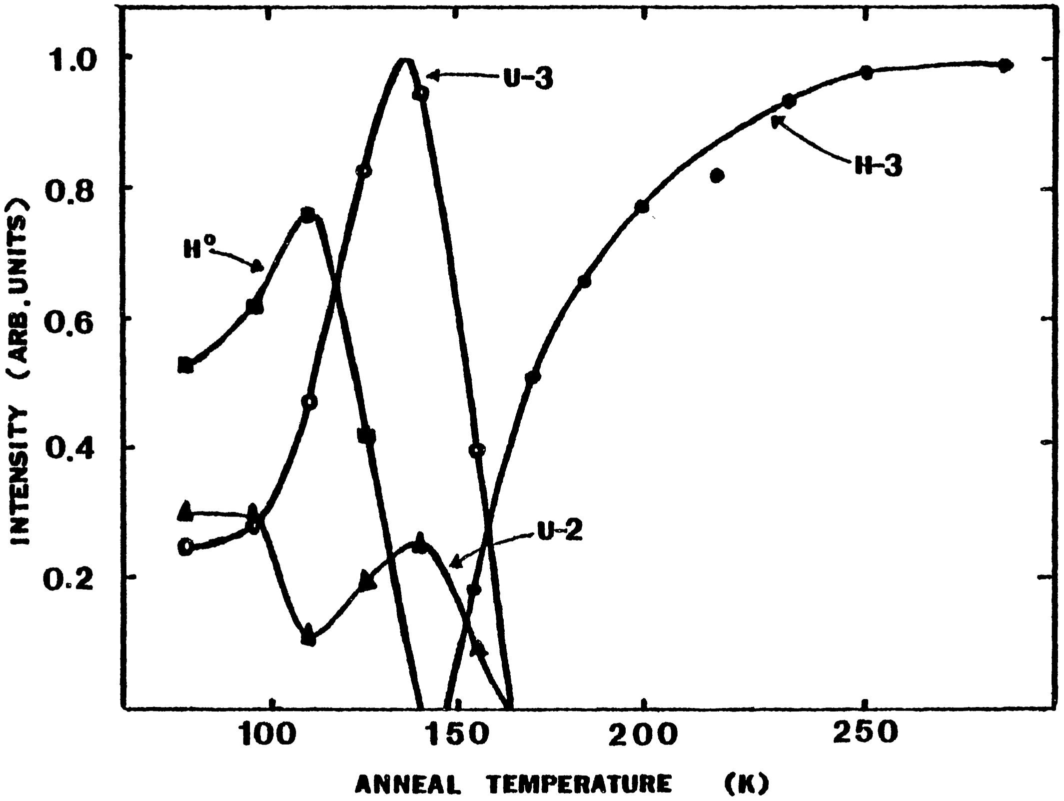

Figure 30. Thermal stability of the U-2, U-3, H^{o}, and H-3 centers . ESR data was taken at 77 K

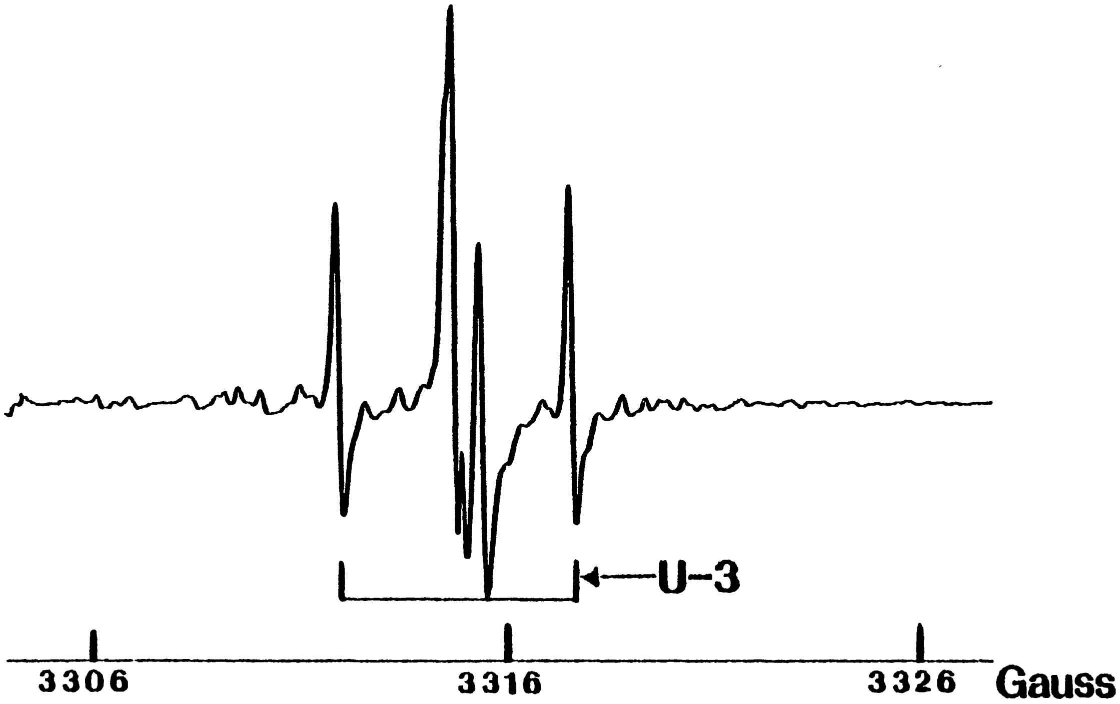

Figure 31. ESR spectra of the U-3 centers when the U-2 centers disappear
The microwave frequency is 9.281504 GHz

before annealing) grew while the U-3 centers decrease. This result is different from the one shown in Figure 30. By comparing these two sets of anneal data, we conclude that rearrangements of the protons can occur between the hydrogen atoms and the U-centers. Clearly, the precursors of the U-2 centers were not eliminated even though the U-2 centers themselves disappeared after being stored in liquid nitrogen for two weeks.

Angular Dependence Study of the U-3 Centers

Because of the overlap of the U-2 and U-3 center spectra at some magnetic angles, an angular dependence study of the U-3 centers was done after the U-2 centers had been eliminated. Table XII lists the uncorrected, corrected, calculated magnetic field values and the microwave frequencies. The corrected magnetic field values and the field correction factors from the standard sample, $MgO:Cr^{3+}$ are listed in Table XIII. The final set of parameters and the computer predicted angular dependent spectra are shown in Table XIV and Figure 32.

Discussion

U-2 and U-3 Centers

The goal of this portion of our investigation was to determine the appropriate models for the U-2 and U-3 centers. Based on the experimental results we obtained, the models for the U-2 and U-3 centers must be consistent with

TABLE XII

ANGULAR DEPENDENT DATA FOR U-3 CENTERS AT 77 K

Angle	Uncorrected Field in Gauss	Corrected Field in Gauss	Calculated Field in Gauss	Microwave Frequency in GHz
-72°	3314.024	3310.860	3310.871	9.2801090
	3314.024	3310.860	3310.901	9.2801090
	3314.402	3311.237	3311.202	9.2801079
	3319.550	3316.380	3316.517	9.2801221
	3319.550	3316.380	3316.576	9.2801221
	3323.190	3320.017	3320.179	9.2801130
-60°	3313.904	3310.780	3310.593	9.2800645
	3314.334	3311.209	3311.133	9.2800934
	3314.334	3311.209	3311.142	9.2800934
	3319.254	3316.125	3316.253	9.2800713
	3319.694	3316.564	3316.710	9.2800710
	3322.828	3319.695	3319.944	9.2800748
-50°	3313.710	3310.574	3310.318	9.2802132
	3314.630	3311.493	3311.279	9.2802185
	3314.630	3311.493	3311.314	9.2802185
	3319.264	3316.123	3316.120	9.2802341
	3319.914	3316.772	3316.808	9.2802123
	3322.496	3319.352	3319.437	9.2802108
-40°	3313.544	3310.384	3310.211	9.2802362
	3314.750	3311.589	3311.364	9.2802341
	3314.750	3311.589	3311.414	9.2802341
	3319.268	3316.103	3316.083	9.2802444
	3320.012	3316.846	3316.882	9.2802477
	3321.956	3318.788	3318.791	9.2802468
-30°	3313.508	3310.309	3310.229	9.2802778
	3314.758	3311.558	3311.318	9.2802682
	3314.758	3311.558	3311.365	9.2802682
	3319.332	3316.128	3316.304	9.2802662
	3320.058	3316.853	3316.922	9.2802550
	3321.356	3318.850	3317.558	9.2802621
-20°	3313.620	3310.372	3310.374	9.2802795
	3314.660	3311.411	3311.194	9.2802843
	3314.660	3311.411	3311.221	9.2802843
	3319.476	3316.222	3316.533	9.2802841
	3320.052	3316.798	3316.883	9.2802774
	3320.760	3317.505	3317.101	9.2802739

TABLE XII (continued)

Angle	Uncorrected Field in Gauss	Corrected Field in Gauss	Calculated Field in Gauss	Microwave Frequency in GHz
-10^0	3313.858	3310.569	3310.643	9.2802886
	3314.464	3311.174	3311.194	9.2802819
	3314.464	3311.174	3311.221	9.2802819
	3319.660	3316.365	3316.533	9.2802934
	3319.980	3316.685	3316.883	9.2802785
	3320.254	3316.958	3317.101	9.2802779
0^0	3314.206	3311.939	3311.019	9.2802670
	3319.878	3316.606	3316.809	9.2802592
$+10^0$	3313.322	3310.489	3310.782	9.2796822
	3313.322	3310.489	3310.812	9.2796822
	3314.018	3311.184	3311.465	9.2796787
	3319.132	3316.294	3316.708	9.2796791
	3319.132	3316.294	3316.709	9.2796791
	3319.500	3316.661	3317.110	9.2796791
$+25^0$	3313.000	3310.195	3310.423	9.2796827
	3313.000	3310.195	3310.489	9.2796827
	3314.476	3311.939	3312.152	9.2796841
	3319.040	3316.230	3316.539	9.2796956
	3319.352	3316.542	3316.929	9.2796935
	3319.894	3317.083	3317.496	9.2796869
$+30^0$	3312.914	3310.130	3310.317	9.2797039
	3312.914	3310.130	3310.390	9.2797039
	3314.964	3312.178	3312.358	9.2796984
	3318.996	3316.207	3316.484	9.2797016
	3319.528	3316.739	3317.095	9.2796988
	3320.000	3317.210	3317.602	9.2796967
$+35^0$	3312.826	3310.070	3310.223	9.2796941
	3312.826	3310.070	3310.301	9.2796941
	3315.150	3312.392	3312.541	9.2796918
	3318.958	3316.197	3316.433	9.2796897
	3319.744	3316.982	3317.301	9.2796893
	3320.070	3317.308	3317.690	9.2796881
$+50^0$	3312.668	3309.966	3310.041	9.2796775
	3312.668	3309.966	3310.126	9.2796775
	3315.474	3312.769	3312.904	9.2796810
	3318.836	3316.128	3316.316	9.2796778
	3320.156	3317.447	3317.805	9.2796791
	3320.556	3317.847	3318.083	9.2796824

TABLE XII (continued)

Angle	Uncorrected Field in Gauss	Corrected Field in Gauss	Calculated Field in Gauss	Microwave Frequency in GHz
+60°	3312.642	3309.937	3310.021	9.2796859
	3312.642	3309.937	3310.113	9.2796859
	3315.502	3312.794	3312.957	9.2796855
	3318.776	3316.066	3316.279	9.2796758
	3320.090	3317.379	3317.741	9.2796798
	3321.182	3318.470	3318.663	9.2796733
+70°	3312.674	3309.960	3310.086	9.2796853
	3312.674	3309.960	3310.185	9.2796853
	3315.322	3312.605	3312.846	9.2796924
	3318.732	3316.013	3316.280	9.2796798
	3319.908	3317.188	3317.571	9.2796810
	3321.774	3319.052	3319.211	9.2796782

TABLE XIII

FIELD-CORRECTION FACTORS AS DETERMINED FROM STANDARD $MgO:Cr^{3+}$ SAMPLE FOR U-3 CENTERS AT 77 K

Degrees	$(H_{Cr^{3+}})$	Microwave Frequency (GHz)	ΔH
-72^0	3352.532	9.2812941	3.201
-60^0	3352.494	9.2813012	3.161
-50^0	3352.506	9.2813005	3.173
-40^0	3352.534	9.2813107	3.197
-30^0	3352.576	9.2813188	3.236
-20^0	3352.624	9.2813131	3.286
-10^0	3352.664	9.2813090	3.328
0^0	3352.638	9.2813015	3.305
$+10^0$	3351.756	9.2800719	2.856
$+20^0$	3351.756	9.2800998	2.816
$+30^0$	3351.716	9.2800992	2.788
$+40^0$	3351.684	9.2800879	2.734
$+50^0$	3351.638	9.2801106	2.737
$+60^0$	3351.644	9.2801106	2.737
$+70^0$	3351.642	9.2800884	2.746

TABLE XIV

SPIN-HAMILTONIAN PARAMETERS FOR U-3 CENTERS AS DETERMINED AT 77 K

		θ	ϕ
g_x	2.0008	162.2	142.0
g_y	1.9995	97.7	27.2
g_z	2.0016	106.0	295.0
A_x	12.6	33.0	175.6
A_y	15.6	79.7	281.8
A_z	26.2	59.0	18.0

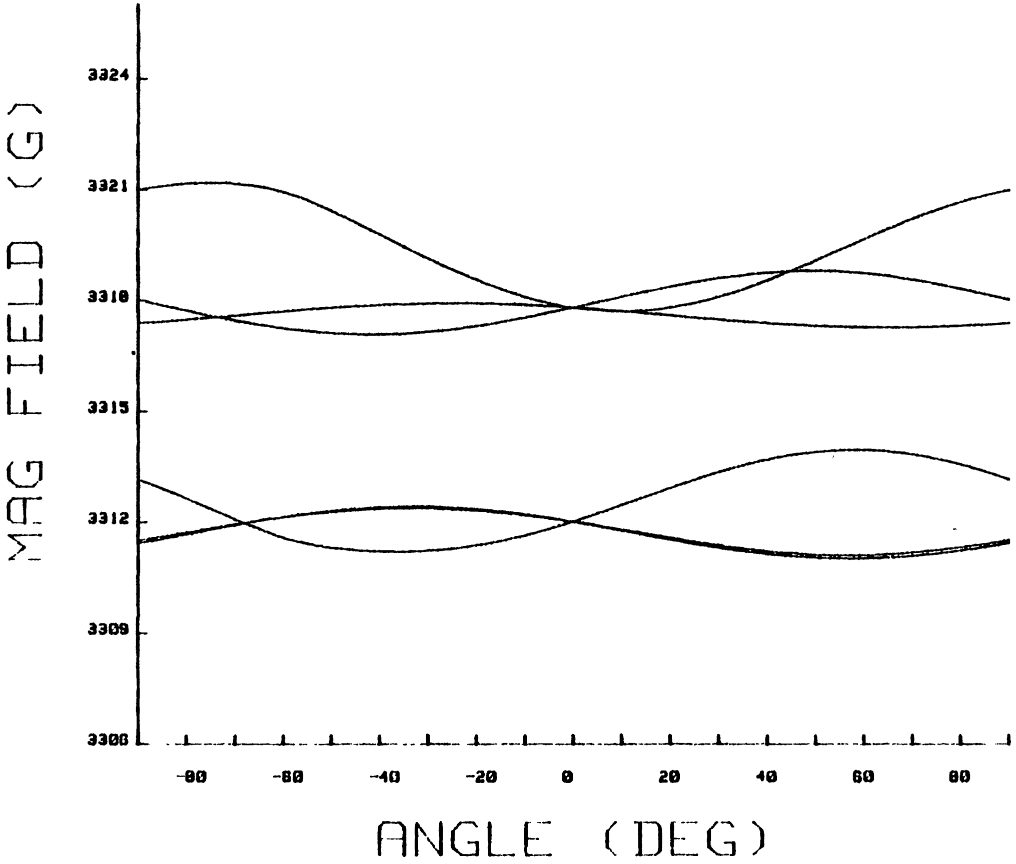

Figure 32. Computer predicted angular dependence of the U-3 centers at 77 K

the following observations: (1) the production curves for these centers do not saturate until very high doses of radiation (greater than 100 Megarads), (2) they are electronlike because of their negative g shifts, (3) they contain a single proton as shown by electron-nuclear double resonance (ENDOR) experiments and by ESR spin-flip transitions, (4) their long spin-lattice relaxation times indicates rapid reorientations of electrons or ions within the defect, (5) they inter-convert and both increase when the hydrogen atoms decay, and (6) the unpaired electron in each defect is localized primary on one silicon ion.

The localization of the unpaired electron on a single silicon ion suggests two possible models, one involving an oxygen vacancy such as the E-type centers and the other involving no vacancy. Thus, for the U-2 and U-3 centers, we propose a model which is similar to the $[SiO_4/Li^+]^\circ$ center recently described by Jani et al. (52). This latter center consists of an interstitial lithium ion adjacent to a Si^{4+} ion. The essential aspect of the defect is trapping an electron on a silicon ion, thus forming the Si^{3+} ion, and having a nearby entity to provide charge compensation for the trapped electron. In the case of Jani et al. (52), the compensator is the interstitial lithium ion. Whereas, in the case of the U-2 and U-3 centers, an interstitial proton in the form of an OH^- molecule would provide the charge compensation for an extra electron trapped on a silicon ion. We propose the more descriptive labels of $[SiO_4/H^+]^\circ_1$ and

$[SiO_4/H^+]^\circ_2$ for the U-2 and U-3 centers. In summary, the $[SiO_4/Li^+]^\circ$ centers and the $[SiO_4/H^+]^\circ$ centers have a number of similar properties: (1) they are only stable at low temperature, (2) they both have similar negative g shifts, (3) they are defects with nearby interstitial compensators (Li^+ or H^+), and (4) they have similar large hyperfine interactions (~400 G) due to one ^{29}Si.

The proposed model for the U-2 and U-3 centers is shown in Figure 33. Basically, this model is equivalent to a hydrogen atom except that the electron is localized on the silicon instead of the proton which, in turn, allows the proton to form an OH^- molecule with one of the adjacent oxygen ions. The difference between the U-2 and U-3 centers occurs because the OH^- molecule is on a long bond side of the Si^{3+} in one case and on a short bond side in the other case. Hopping of the proton between the two differently bonded oxygens would account for the interconversions of the two defects. We also believe that the thermal decay of the hydrogen atoms into separate protons and electrons will allow more U-2 and U-3 centers to be formed.

Again, it must be emphasized that these proposed models for the U-2 and U-3 centers have not been absolutely established. Further analysis of the angular dependence data presented in this chapter and future studies of the angular dependence of the ^{29}Si hyperfine interactions will help to prove or disprove these models.

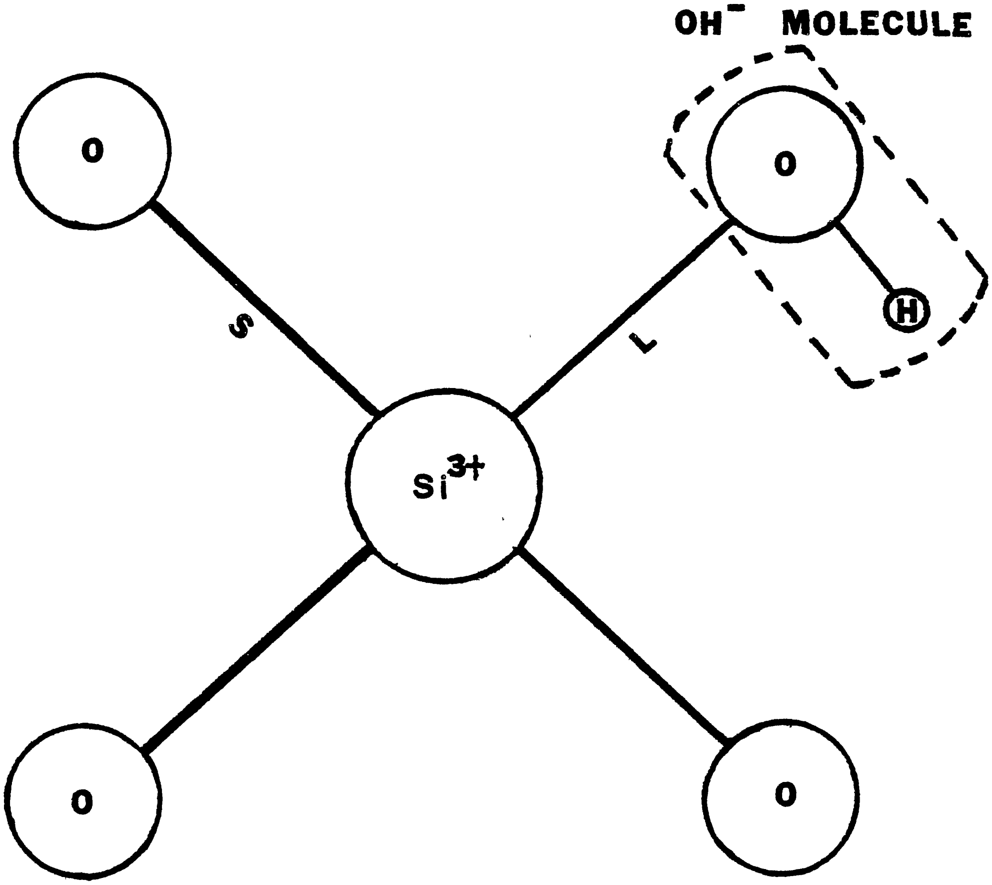

Figure 33. Proposed model for the U-2 and U-3 centers

REFERENCES

(1) Evans, R.C., Crystal Chemistry, University Press Cambridge, (1964).

(2) Megaw, H.D., Crystal Structures: A Working Approach, W.B. Saunders Company (1973).

(3) Cady, W.G., Piezoelectricity, Dover Company, New York, (1964).

(4) Halliburton, L.E., J.J. Martin, and D.R. Koehler, Precision Frequency Control, Academic Press, New York, (1985).

(5) Nuttal, R.H.D., and J.A. Weil, Can. J. Phys., 59, 1696 (1981).

(6) King, J.C., Bell Syst. Tech. J., 38, 573 (1959).

(7) Pellegrini, P., E. Euler, A. Kahan, T.M. Flanagan, and T. Wrobel, IEEE Trans. on Nuc. Sci., NS-25, 1267 (1978).

(8) Weeks, R.A., J. of Appl. Phys., 27, 1376 (1956).

(9) Weeks, R.A., and C.M. Nelson, J. Am. Ceram. Soc. 43 399 (1960).

(10) Silsbee, R.H., J. of Appl. Phys., 32, 1459 (1961).

(11) Feigl, F.J., W.B. Fowler, and K.L. Yip, Solid State Commun., 14, 225 (1974).

(12) Yip, K.L., and W.B. Fowler, Phys. Rev. B, 11, 2327 (1975).

(13) Jani, M.G., R.B. Bossoli, and L.E. Halliburton, Phys. Rev. B, 27, 2285 (1983).

(14) Weeks, R.A., Phys. Rev., 130, 570 (1963).

(15) Jani, M.G., MS Thesis, Oklahoma State University, (1979).

(16) Haberlandt, H., Int. Wiss. Kollog. Tech., Hochschule Ilmenau (East Germany), 20, 13 (1975).

(17) Solentsev, V.P., R.I. Mashkovtsev, and M.Ya. Shcherbakova, J. Struct. Chem. (USSR), 18, 578 (1977).

(18) Halliburton, L.E., B.D. Perlson, R.A. Weeks, J.A. Weil, and M.C. Wintersgill, Solid State Commun., 30, 575 (1975).

(19) Isoya, J., J.A. Weil, and L.E. Halliburton, J. Chem. Phys., 74, 10 (1981).

(20) Weeks, R.A. and M.M. Abraham, Bull. AM. Phys. Soc., 10, 374 (1965).

(21) Bossoli, R.B., M.G. Jani, and L.E. Halliburton, Solid State Commun., 44, 213 (1982).

(22) Jani, M.G., Ph.D. Dissertation, Oklahoma State University, (1982).

(23) Halliburton, L.E., Review Paper, (in press), (1985).

(24) Weil, J.A., Phys. Chem. Minerals, 10, 149 (1984).

(25) Griffiths, J.H.E., J. Owen, and I.M. Ward, Nature, 173, 439 (1954).

(26) O'Brien, M.C.M., Proc. Roy. Soc. (London), A231 404 (1955).

(27) Schnadt, R. and J. Schneider, Phys., 62, 21 (1984).

(28) Nuttal, R.H.D. and J.A. Weil, Can. J. Phys., 62, 21 (1984).

(29) Schnadt, R. and A. Rauber, Solid State Commun., 9, 159 (1971).

(30) Schirmer, O.F., Solid State Commun., 18, 1349 (1976).

(31) Nuttal, R.H.D. and J.A. Weil, Solid State Commun., 35, 789 (1980).

(32) Halliburton, L.E., N. Koumvakalis, M.E. Markes, and J.J. Martin, J. Appl. Phys., 52, 3565 (1981).

(33) Barker, P.R., J. Phys. C, 8, L142 (1975).

(34) Mckeever, S.W.S, Radiation Protection Dosimetry, 8, 81 (1984).

(35) Markes, M.E. and L.E. Halliburton, J. Appl. Phys., 50, 8172 (1979).

(36) Martin, J.J., J. Appl. Phys., 56, 2536 (1984).

(37) Martin, J.J., H.B. Hwang, and H. Bahadurr, Proc. Annual 39th Frequency Control (in press), (1985).

(38) Mackey, Jr. J.H., The J. of Chem. Phys., 39, 74 (1963).

(39) Nuttal, R.H.D. and J.A. Weil, Can. J. Phys., 39, 1709 (1981).

(40) Mckeever, S.W.S, C.Y. Chen, and L.E. Halliburton, Proc. Nuclear Tracks, (in press), (1985).

(41) Nuttal, R.H.D. and J.A. Weil, Can. J. Phys., 59, 1886 (1981).

(42) Zavoisky, E., J. Phys., U.S.S.R., 9, 211, 245 (1945).

(43) Wertz, J.E. and J.R. Bolton, Electron Spin Resonance: Elementary Theory and Practical Applications, Mcgraw Hill book company New York, (1973).

(44) Poole, C.P. Jr. and H.A. Farach, The Theory of Magnetic Resonance, John Wiley & Sons, Inc. New York, (1972).

(45) Abragam, M.M. and B. Bleaney, Electron Paramagnetic Resonance of Transition Ions, Clarendon Press, Oxford, (1970).

(46) Poole, C.P. Jr., Electron Paramagnetic Resonance: A Comprehensive Treatise on Experimental Techniques, John Wiley & Sons, Inc. New York, (1983).

(47) Fermi, E., Z. Physik, 60, 320 (1930).

(48) Norton, J.R., J.M. Cloeren, and J.J. Suter, Proc. Annual 38th Frequency Control, 63, (1984).

(49) Isoya, J., J.A. Weil, and R.F.C. Claridge, J. Chem. Phys., 69, 4876 (1978).

(50) Jani, M.G., L.E. Halliburton, and E.E. Kohnke, J. Appl. Phys., 54, 6321 (1983)

(51) Nuttall, R.H.D. and J.A. Weil, Solid State Commun., 33, 99 (1980)

(52) Jani, M.G., L.E. Halliburton, and A. Halperin, to be published.

VITA

Ching-Yuan Chen

Candidate for the Degree of

Doctor of Philosophy

Thesis: ELECTRON SPIN RESONANCE OF POINT DEFECTS IN QUARTZ

Major Field: Physics

Biographical:

Personal Data: Born in Tainan, Taiwan, R.O.C., March 1, 1950, the son of Mr. and Mrs. Y.C. Chen.

Education: Graduated from Tainan First High School, in June, 1969; received Bachelor of Science degree in Applied Mathematics from National Taiwan Chung Hsing University in June, 1973; served in the army in Taiwan from 1973 to 1975; graduate study in the Department of Physics of National Taiwan University from 1977 to 1978 and graduate study in the Department of Physics of University of Arkansas in the spring of 1979; received Master of Science degree from Oklahoma State University in July, 1982; completed requirements for the Doctor of Philosophy degree at Oklahoma State University in December, 1985.